UNIVERSITY OF TORONTO

DEPARTMENT OF CHEMICAL ENGINEERING
AND APPLIED CHEMISTRY

NUMERICAL SIMULATION
OF
STEAM INJECTION IN BITUMEN
AND HEAVY OIL RESERVOIRS
PHASE I: PART 2

Development of a Methodology for a 2-Dimensional Dynamic Grid Simulator

PART 2

Prepared for
The Department of Energy, Mines and Resources, Canada
under contract OST83-00195
22ST-23440-3-9168

by
Peter G. DeBuda
and
Donald E. Cormack
Department of Chemical Engineering
and Applied Chemistry
University of Toronto

76 pp

September, 1986

MICROMEDIA

ABSTRACT

The one-dimensional steam injection simulator, developed in part I of this work to track the movement of the steam front as it progresses through a one-dimensional core, is extended to two dimensions. The technique for handling the dynamic grid, and the block-balance method used to develop the finite-difference approximation to the governing equations, boundary conditions, and matching conditions (at the steam front) are described in considerable detail.

Some preliminary numerical results are presented for the two-dimensional simulation. It was found that the Jacobian matrix tended to be ill-conditioned under certain circumstances and still requires some additional work to clarify the causes of the ill-conditioning. As yet, the simulator is not able to track the steam front past stationary grid points. This limitation of the simulator is not fundamental, and can be remedied with further work.

An extensive survey of the open literature describing the physical properties of the Cold Lake heavy oil deposit, required for the numerical simulation of the oil recovery process, was also carried out. Tables of reported properties are provided in the report, and values considered representative are summarized.

4. THE FRONT-TRACKING METHOD

4.1 Introduction

Numerical simulation has become an essential tool in the design and economic assessment of oil recovery strategies. Numerical simulation studies are particularly important as more sophisticated and costly recovery schemes are contemplated. Heavy oil and bitumen recovery by thermal in situ methods is a case in point.

A problem which plagues essentially all steam injection simulators which have been presented in the literature, is spurious injection pressure or injection rate oscillations in time. The problem is particularly apparent in one-dimensional simulations. Although less obvious in two- and three-dimensional simulations, the inherent causes of the spurious oscillations in the one-dimensional case (i.e. the finite-difference representation of the governing equations) are still present in the higher-dimensional problems. Hence, errors in predicted reservoir performance are expected to persist in two and three dimensions.

To overcome the injection rate/injection pressure problem, a numerical simulator which tracks the location of the steam front and explicitly solves for the state variables at the steam front was developed. This simulator, which was restricted to simulations in one spatial dimension, is described in part I of this report. Although some oscillation of injection well variables was still observed in the front-tracking simulations, the magnitude of the oscillations was reduced considerably, to the extent that the attempt was considered successful.

Part II of this report describes progress toward the extension of the front-tracking approach to two spatial dimensions. The purpose of this extension is to develop a simulator which is able to perform better, in situations with sharp steam fronts, than existing simulators. It is expected that such a simulator, which

maintains a clear demarcation of the steam front, will provide superior performance in heavy oil and bitumen reservoirs in which a steam chamber is developed as a result of relatively low pressure steam injection, as is presently being done in the horizontal well processes in Cold Lake. The numerical technique might ultimately be developed into an adaptive grid approach which will allow a finer numerical solution mesh to be used near the steam front where state variable gradients are largest.

In the following, a two-dimensional front-tracking approach is developed.

4.2 The Finite-Difference Grid

As a starting point for the technical discussion, we shall describe the grid system which was chosen to represent the continuum equations in finite-difference form. This will make easier the subsequent discussion of the equations themselves.

The grid system adopted consists of a standard stationary rectangular grid plus a set of front-tracking grid points constrained to move along the horizontal and vertical grid lines as the front moves. An example is shown in figure 4.1. The set of front-tracking points may be interpreted as the set of intersections between the grid lines (both horizontal and vertical) and a "simple" curve which extends from one point on the boundary of the grid to a different point on the boundary of the grid. (For our purposes, a "simple" curve is a curve which does not intersect itself, and which does not enter and leave any grid block more than once.) The line segments joining the front-tracking grid points constitute an approximate description of the location of the steam front. Since front-tracking grid points have been placed on both horizontal and vertical grid lines, horizontal, vertical and diagonal steam fronts can all be simulated with this grid.

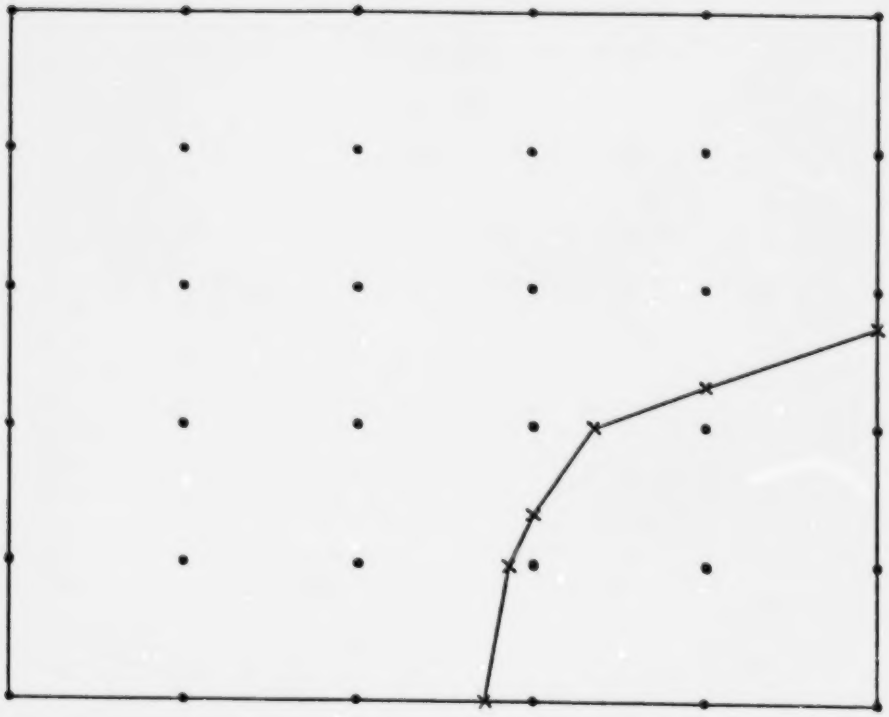

FIGURE 4.1. A typical grid with front-tracking points.

For reasons which are discussed at the beginning of the next section, we have chosen to discretize the governing differential equations using block balances. Hence, it is necessary to identify clearly the grid blocks, particularly in the vicinity of the front-tracking points.

The method of dividing the region into grid blocks is more complicated than it would be if no front-tracking grid points had been added. Since the saturations of oil, water and vapour on the two sides of the steam front are significantly different, the steam front should constitute a boundary between grid blocks. Furthermore, since the presence of very small grid blocks is detrimental to the numerical performance of the simulator, it is necessary to define grid block boundaries such that small block fragments are merged with neighbouring blocks on the same side of the steam front. A method of region division into grid blocks has been devised such that

i) the line segments of the steam front coincide with grid block boundaries,

ii) there is exactly one grid block for each stationary grid point,

iii) adjacent stationary grid points lie in adjacent grid blocks,

iv) diagonally adjacent stationary grid points lie in diagonally adjacent grid blocks, and

v) none of the grid blocks are very small.

The algorithm for constructing the grid blocks has several parts. Figures 4.2 through 4.6 illustrate the grid block boundaries which result after each part of this algorithm is applied to the grid and the front-tracking points shown in figure 4.1. The two small loops on the grid borders in figures 4.3 through 4.5 depict minor inconsistencies in the grid block boundaries. These inconsistencies are removed in part 5 of the algorithm, as figure 4.6 shows.

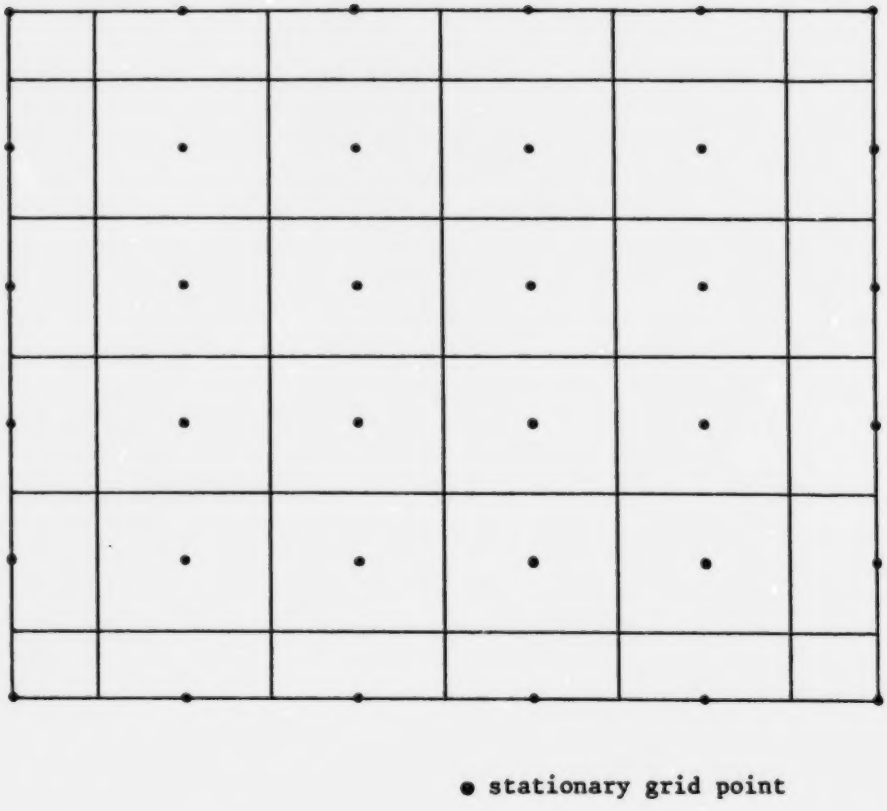

FIGURE 4.2. The grid blocks after part 1 of the partitioning algorithm has been done.

Part 1:

1. Let $X_1, X_2, \ldots, X_{N_X}$ denote the locations of the vertical grid lines.

2. Let $Y_1, Y_2, \ldots, Y_{N_Y}$ denote the locations of the horizontal grid lines.

(Thus, the stationary grid points are located at (X_i, Y_j), $i=1, \cdots, N_X$, $j=1, \cdots, N_Y$).

3. Define

$$X_{i+\frac{1}{2}} = \begin{cases} X_1, & i=0 \\ \frac{1}{2}(X_i+X_{i+1}), & i=1, \cdots, N_X-1 \\ X_{N_X}, & i=N_X \end{cases}$$

and

$$Y_{j+\frac{1}{2}} = \begin{cases} Y_1, & j=0 \\ \frac{1}{2}(Y_j+Y_{j+1}), & j=1, \cdots, N_Y-1 \\ Y_{N_Y}, & y=N_Y \end{cases}$$

4. For each stationary grid point at (X_i, Y_j), $i=1, \cdots, N_X$, $j=1, \cdots, N_Y$, construct a polygonal grid block with corners as follows:

Top-East	$(X_{i+\frac{1}{2}}, Y_{j+\frac{1}{2}})$
Top-Middle	$(X_i, Y_{j+\frac{1}{2}})$
Top-West	$(X_{i-\frac{1}{2}}, Y_{j+\frac{1}{2}})$
West	$(X_{i-\frac{1}{2}}, Y_j)$
Bottom-West	$(X_{i-\frac{1}{2}}, Y_{j-\frac{1}{2}})$
Bottom-Middle	$(X_i, Y_{j-\frac{1}{2}})$
Bottom-East	$(X_{i+\frac{1}{2}}, Y_{j-\frac{1}{2}})$
East	$(X_{i+\frac{1}{2}}, Y_j)$

Some of these corners will be changed in the remaining steps of the algorithm, unless there are no front-tracking points in the grid.

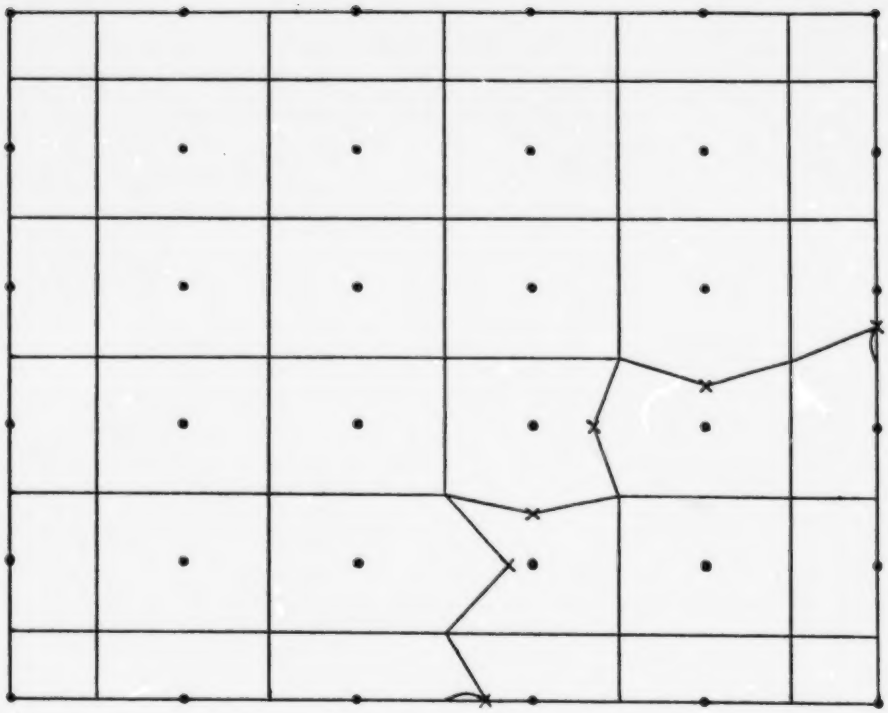

. stationary grid point

x front-tracking point

FIGURE 4.3. The grid blocks after part 2 of the partitioning algorithm has been done.

Part 2:

For each front-tracking grid point,

1. Determine whether it is on a horizontal or vertical grid line.

   If the front-tracking point is on a *horizontal* grid line:

   2. Determine i,j such that the front-tracking point is between grid points (i,j) and (i+1,j).

   3. Redefine both the east corner of grid block (i,j) and the west corner of grid block (i+1,j) to coincide with the front-tracking point.

   If the front-tracking point is on a *vertical* grid line:

   2. Determine i,j such that the front-tracking point is between grid points (i,j) and (i,j+1).

   3. Redefine both the top-middle corner of grid block (i,j) and the bottom-middle corner of grid block (i,j+1) to coincide with the front-tracking point.

Whether the grid line is horizontal or vertical:

4. Record that the two corners have been redefined.

Part 3:

(It is assumed that the front-tracking grid points have been ordered so that point m is located between point m-1 and point m+1 on the steam front.)

For each front-tracking point, m, except the last one (which is numbered N_F):

1. Determine i,j such that both that particular front-tracking point (m) and the next front-tracking point (m+1) are located on the rectangle with stationary grid points (i,j), (i+1,j), (i,j+1), and (i+1,j+1). (It follows from the method by which the front-tracking points are selected, as described above, that this

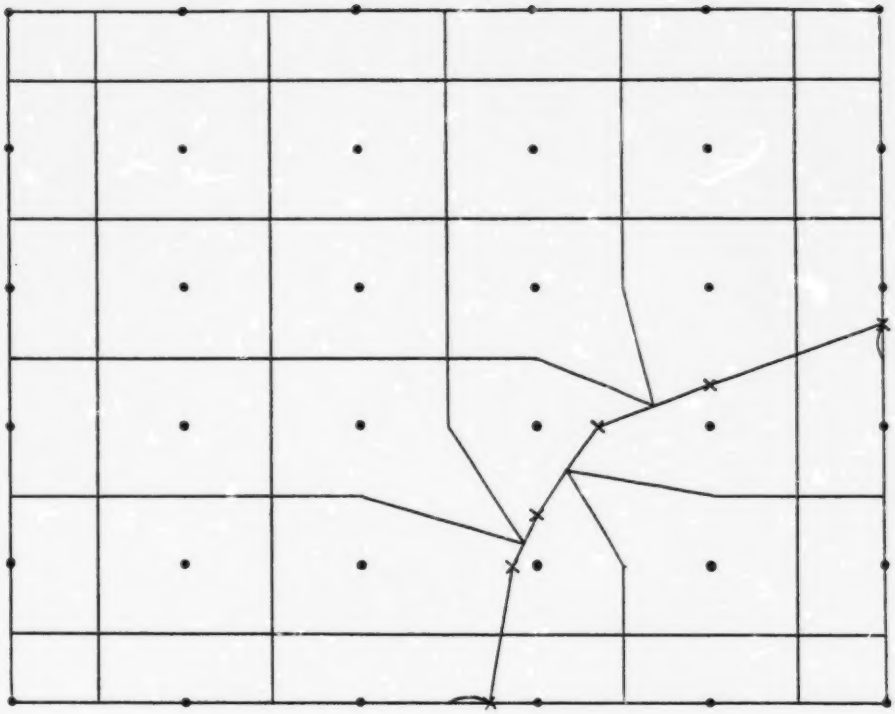

. stationary grid point

x front-tracking point

FIGURE 4.4. The grid blocks after part 3 of the partitioning algorithm has been done.

is always possible, and that i and j are uniquely specified.)

2. Redefine

   the bottom-west corner of grid block (i+1,j+1),

   the bottom-east corner of grid block (i,j+1),

   the top-east corner of grid block (i,j),

   and the top-west corner of grid block (i+1,j)

   to be the midpoint of the line segment joining that particular front-tracking point (m) and the next front-tracking point (m+1).

3. Record that the four corners have been redefined.

Part 4:

For each grid block:

1. If the top-middle corner has not been redefined in part 2 of this algorithm, but exactly one of the top-east or top-west corners has been redefined in part 3, then redefine the top-middle corner so that the top-east, top-middle, and top-west corners are collinear, and the top-middle corner continues to lie on vertical grid line i. For example, the (3,1), (3,2), (4,1), (4,3), and (5,2) grid blocks in figure 4.4 satisfy this condition.

2. If the west corner has not been redefined in part 2 of this algorithm, but exactly one of the top-west or bottom-west corners has been redefined in part 3, then redefine the west corner so that the top-west, west, and bottom-west corners are collinear, and the west corner continues to lie on horizontal grid line j. For example, the (4,3), (5,2), (5,4), (6,3), and (6,4) grid blocks in figure 4.4 satisfy this condition.

3. If the bottom-middle corner has not been redefined in part 2 of this algorithm, but exactly one of the bottom-west or bottom-east corners has been redefined in part 3, then redefine the bottom-middle corner so that the

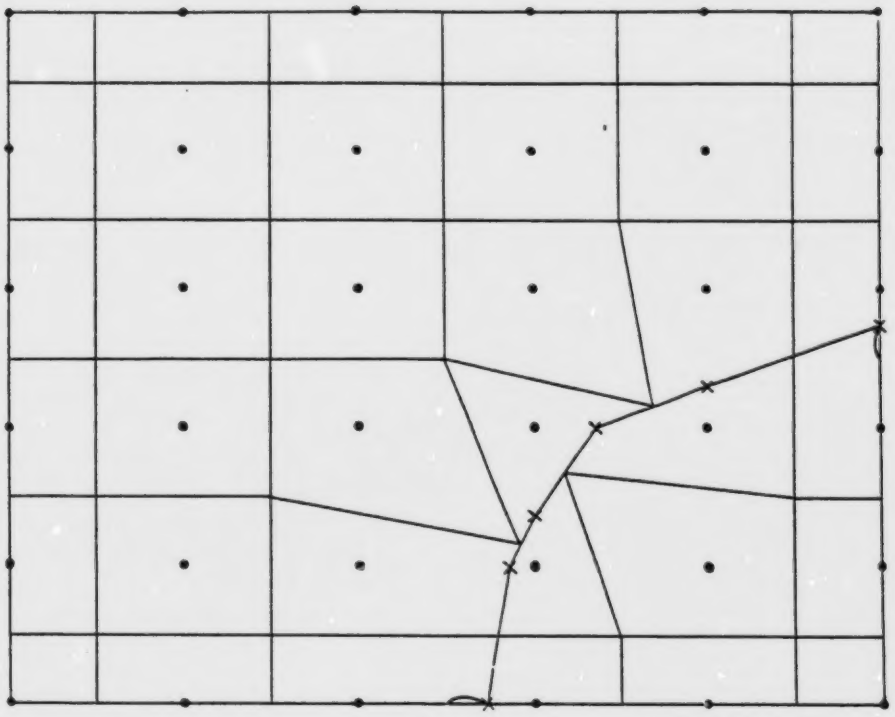

. stationary grid point

x front-tracking point

FIGURE 4.5. The grid blocks after part 4 of the partitioning algorithm has been done.

bottom-west, bottom-middle, and bottom-east corners are collinear, and the bottom-middle corner continues to lie on vertical grid line i. For example, the (3,2), (3,3), (4,2), (4,4), and (5,3) grid blocks in figure 4.4 satisfy this condition.

4. If the east corner has not been redefined in part 2 of this algorithm, but exactly one of the bottom-east or top-east corners has been redefined in part 3, then redefine the east corner so that the bottom-east, east, and top-east corners are collinear, and the east corner continues to lie on vertical grid line j. For example, the (3,3), (4,2), (4,4), (5,3), and (5,4) grid blocks in figure 4.4 satisfy this condition.

Part 5:

1. For each grid block on the bottom border of the grid, redefine the bottom-west corner to coincide with the west corner, and the bottom-east corner to coincide with the east corner.
2. For each grid block on the top border of the grid, redefine the top-west corner to coincide with the west corner, and the top-east corner to coincide with the east corner.
3. For each grid block on the west border of the grid, redefine the bottom-west corner to coincide with the bottom-middle corner, and the top-west corner to coincide with the top-middle corner.
4. For each grid block on the east border of the grid, redefine the bottom-east corner to coincide with the bottom-middle corner, and the top-east corner to coincide with the top-middle corner.

Most of these "redefinitions" (in part 5) have no effect, because the various pairs of corners coincide already after part 1 of this algorithm is completed. However, a side-effect of part 2 (and possibly parts 3 and 4) is that a few of the pairs

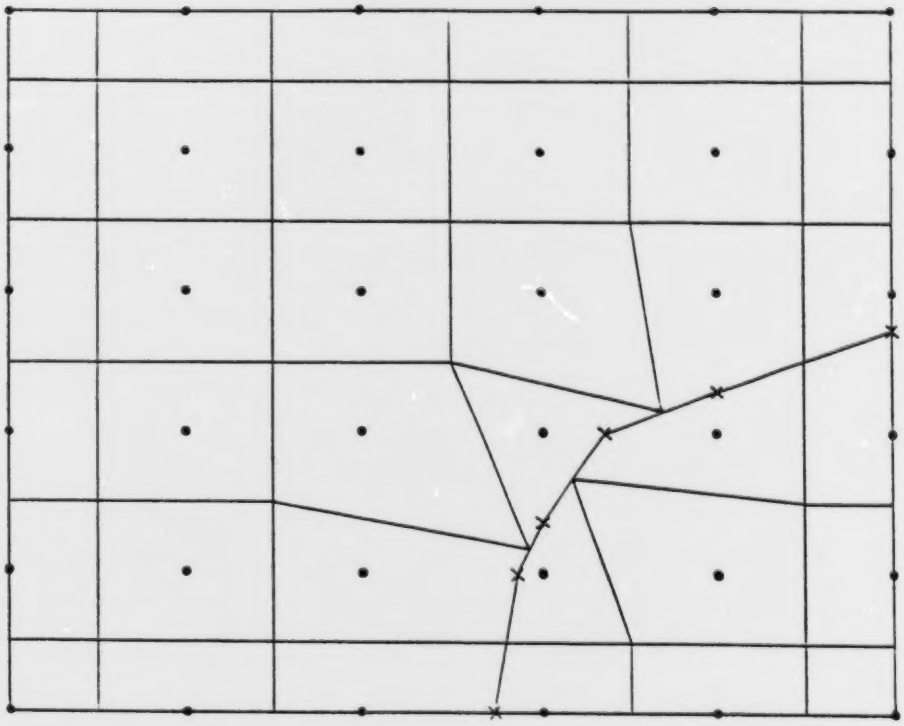

. stationary grid point

x front-tracking point

FIGURE 4.6. The grid blocks after all 5 parts of the partitioning algorithm have been done.

no longer coincide. It is more convenient to perform all the "redefinitions" than to figure out which ones are necessary.

This is the end of the partitioning algorithm.

4.3 Finite-Difference Representation of the Equations

It is apparent from the previous section that irregular grid spacing arises in the vicinity of the front-tracking points. In such a situation, it is extremely difficult to implement a standard finite-difference approximation approach to the governing differential equations. A block-balance method is more readily adapted, and, for uniform grid spacing, yields the same end-result as the standard finite-difference approach.

The task now is to apply the relevant mass and energy balances to the grid blocks as determined in section 4.2. From these balances arise sufficient equations to solve for the locations of all front-tracking points, and for the pressure, temperature, saturations and compositions at all grid points, both stationary and front-tracking.

The system of grid blocks has been set up so that each block has one grid point to itself, which is used to characterize the state of the block, and each front-tracking point is on the boundary between two blocks. All blocks are rectangular except those which touch or are adjacent to the steam front.

The governing equations can be integrated over a typical block, at any moment in time, to obtain the equations

$$\iint_{block}\left[\frac{\partial}{\partial t}(\phi S_p \rho_p w_c) - M_c\right] dX\, dY = \iint_{block} -\nabla\cdot(\tau_p w_c \nabla\Phi_p)\, dX\, dY \qquad (4.01)$$

and

$$\int\int_{block}\left[\frac{\partial}{\partial t}\left(\sum_p \phi S_p \rho_p h_p + (1-\phi)\rho_r h_r\right)\right] dX\, dY$$

$$= \int\int_{block} -\nabla\cdot\left(\sum_p \tau_p h_p \nabla\Phi_p\right) dX\, dY \qquad (4.02)$$

where

$$\Phi_p = P - \rho_p g Y$$

includes the driving force for flow due to pressure, capillary pressure, and gravity. Other variables are defined in the nomenclature. These equations can be combined to eliminate the condensation rates, M_c.

The Gauss divergence theorem can be applied to the right sides of equations (4.01) and (4.02) to obtain

$$\int\int_{block}\left[\frac{\partial}{\partial t}(\phi S_p \rho_p w_c) - M_c\right] dX\, dY = \int_{boundary} -\tau_p w_c \nabla\Phi_p\cdot\underline{n}\, ds \qquad (4.03)$$

and

$$\int\int_{block}\left[\frac{\partial}{\partial t}\left(\sum_p \phi S_p \rho_p h_p + (1-\phi)\rho_r h_r\right)\right] dX\, dY$$

$$= \int_{boundary} -\sum_p \tau_p h_p \nabla\Phi_p\cdot\underline{n}\, ds \qquad (4.04)$$

Equations (4.03) and (4.04) constitute the block balances which ensure conservation of mass and energy respectively.

To this point, no approximations have been made. The most obvious discrete block representation of the left sides of equations (4.03) and (4.04) are

$$\int\int_{A_{ij}}\left[\frac{\partial}{\partial t}(\phi S_p \rho_p w_c) - M_c\right] dX\, dY \approx A_{ij}\left[\frac{\partial}{\partial t}(\phi S_p \rho_p w_c)_{ij} - (M_c)_{ij}\right] \qquad (4.05)$$

and

$$\iint_{A_{ij}} \left[\frac{\partial}{\partial t} \left(\sum_p \phi S_p \rho_p h_p + (1-\phi)\rho_r h_r \right) \right] dX\, dY$$

$$\approx A_{ij} \left[\frac{\partial}{\partial t} \left(\sum_p \phi S_p \rho_p h_p + (1-\phi)\rho_r h_r \right)_{ij} \right] \tag{4.06}$$

where A_{ij} denotes either a grid block or its area, depending on context. These approximations are the block balance analogues of the most prevalent finite-difference approximations in the literature. Unfortunately, these approximations are not well suited to the present simulator, since A_{ij} is not constant for those grid blocks adjacent to the steam front. In this case, a discretization based on equations (4.05) and (4.06) leads to unacceptable mass balance discrepancies.

The above mass balance error can be avoided if equations (4.03) and (4.04) are also integrated over a time step, t^{n-1} to t^n, before they are expressed in finite-difference form. The resulting equation for the mass balances becomes

$$\int_{t^{n-1}}^{t^n} \left\{ \iint_{A_{ij}^n} \left[\frac{\partial}{\partial t} (\phi S_p \rho_p w_c) - M_c \right] dX\, dY \right\} dt$$

$$= \int_{t^{n-1}}^{t^n} \left\{ \int_{b_{ij}^n} -\tau_p w_c \nabla \Phi_p \cdot \underline{n}\, ds \right\} dt \tag{4.07}$$

where b_{ij}^n denotes the boundary of element i,j at time t^n. The integrated enthalpy balance takes a similar form.

The right sides can be approximated by the standard backward-difference formula

$$\textit{(right side of equation (4.07))} \approx (t^n - t^{n-1}) \int_{b_{ij}^n} -\tau_p w_c \nabla \Phi_p \cdot \underline{n}\, ds \tag{4.08}$$

The integral on the left side of equation (4.07) is taken over the block i,j as it is configured at time n. At time n-1, however, block i,j had a different shape. Hence, the representation of this integral is somewhat complicated. It is

$$\textit{(left side of equation (4.07))} = -\int_{t^{n-1}}^{t^n}\iint_{A_{ij}^n} M_c\, dX\, dY\, dt$$

$$+\iint_{A_{ij}^n}(\phi S_p\rho_p w_c)^n\, dX\, dY - \iint_{A_{ij}^n}(\phi S_p\rho_p w_c)^{n-1}\, dX\, dY \qquad (4.09)$$

Equation (4.09) contains three different types of terms which require further representation. The first type is the integral which has M_c as the integrand; it requires no further attention since it will ultimately be eliminated through algebraic manipulation. The second is the integral at time t^n. For this, the straightforward approximation is appropriate:

$$\iint_{A_{ij}^n}(\phi S_p\rho_p w_c)^n\, dX\, dY \approx A_{ij}^n(\phi S_p\rho_p w_c)_{ij}^n \qquad (4.10)$$

The integral at time t^{n-1} is a little more complicated because the integrands for the blocks which change size during a time step are discontinuous. The required expression is

$$\iint_{A_{ij}^n}(\phi S_p\rho_p w_c)^{n-1}\, dX\, dY$$

$$\approx \left[A_{ij}^n - \sum_{k,l}\delta A_{ijkl}^n\right](\phi S_p\rho_p w_c)_{ij}^{n-1} + \sum_{k,l}\delta A_{ijkl}^n(\phi S_p\rho_p w_c)_{kl}^{n-1}$$

$$= A_{ij}^n(\phi S_p\rho_p w_c)_{ij}^{n-1} + \sum_{k,l}\delta A_{ijkl}^n\left[(\phi S_p\rho_p w_c)_{kl}^{n-1} - (\phi S_p\rho_p w_c)_{ij}^{n-1}\right] \qquad (4.11)$$

where δA_{ijkl}^n denotes the area of that part of A_{ij}^n which belonged to block k,l at t^{n-1}, but belongs to block i,j at t^n. Note that δA_{ijkl}^n can be zero, but not negative.

The boundary integral in equation (4.08) must still be represented in discrete form. For the most general case of an arbitrary trapezoidal block, as might occur at the front, we divide the boundary into eight edge segments, as depicted in figure 4.8. The integral can be expressed as the sum of eight integrals, one over each edge segment. Each of these integrals is approximated by an expression in

terms of pressures, temperatures, saturations, and compositions at grid point i,j and at neighbouring grid points. The details of this approximation are explained in section 4.6.

The mathematical development of the enthalpy equation is directly analogous with the mathematical development of the material balances, as described above.

4.4 Finite-Difference Representation of the Matching Conditions

The finite-difference approximations for the matching conditions at the steam front are likewise derived using a block-balance approach. After discretization, the steam front is represented as a set of N_F front-tracking grid points, together with the line segments which connect each front-tracking grid point with its one or two neighbouring front-tracking points. (The two endpoints have only one neighbour each; all the other front-tracking points have two neighbours each.)

Since the flows may be discontinuous at the steam front, it is convenient to define the discretization so that each pair of neighbouring front-tracking grid points is connected by *two* parallel line segments separated by an infinitesimal distance, as shown in figure 4.9 . The front edge segments are then constructed as the two halves of each line segment separated by the midpoint of the line segment. Therefore, there are four front edge segments between each pair of front-tracking points, and, if two null front edge segments (of zero length) are assigned to each of the two endpoint front-tracking points, four front edge segments touch each front-tracking point.

It is often convenient to regard the front edge segments which touch a front-tracking point as the edge segments of a degenerate grid block with zero area, of

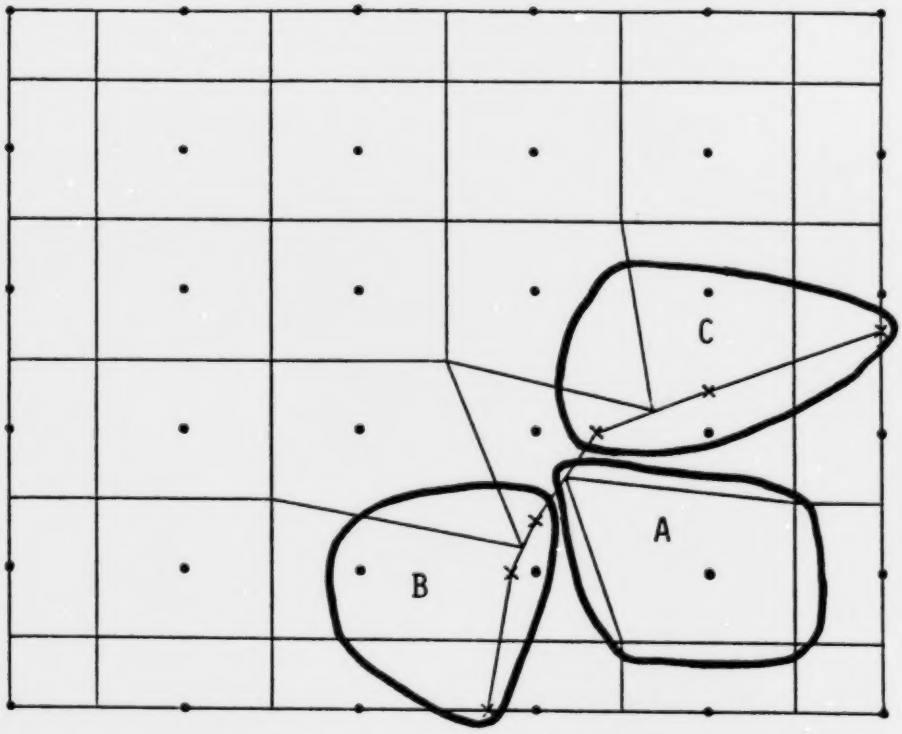

FIGURE 4.7. The context for figures 4.8 and 4.9. The grid blocks are the same as in Figure 4.6.

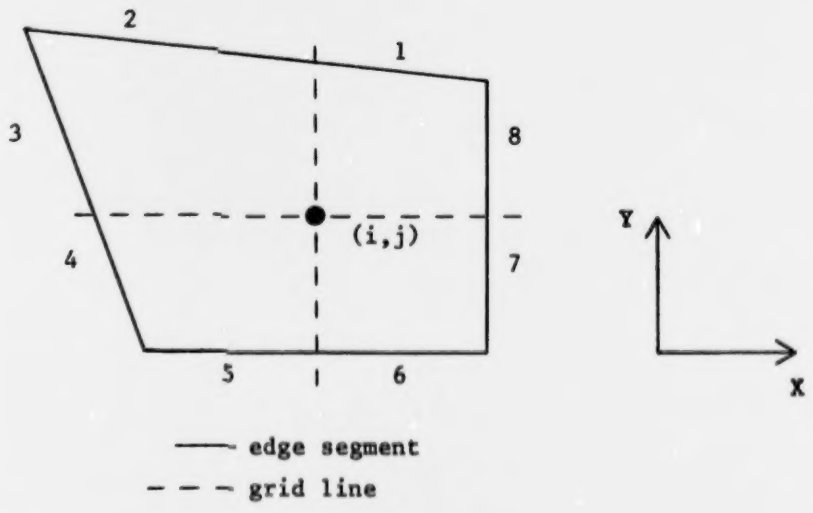

FIGURE 4.8. The 8 edge segments of a typical grid block. This diagram provides a more detailed description of area A in figure 4.7.

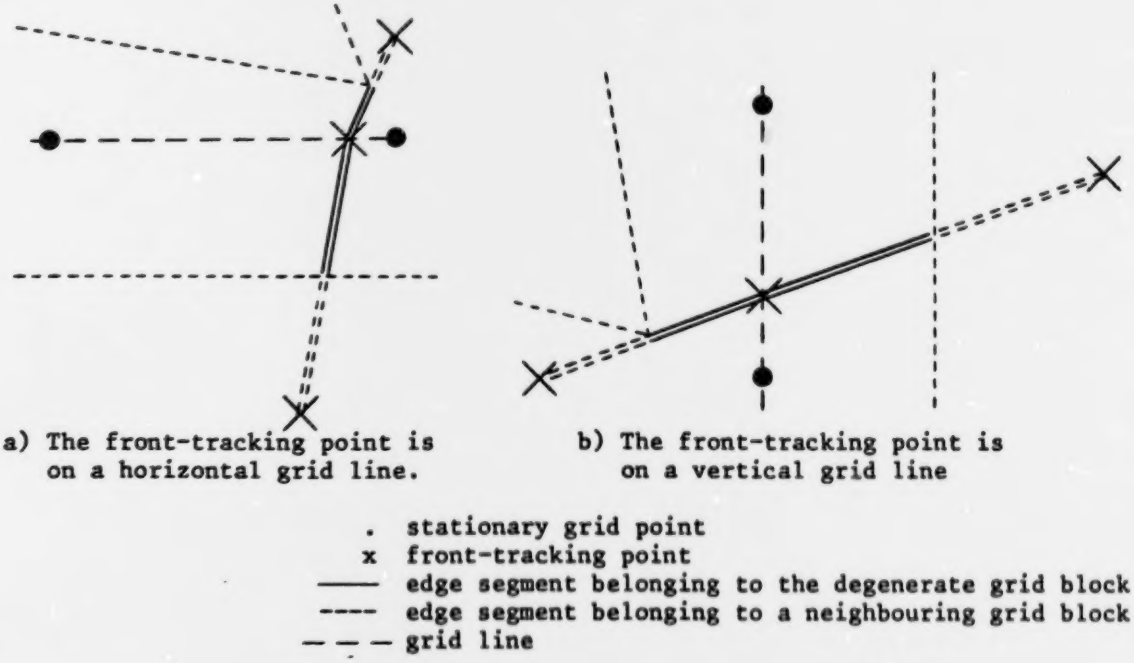
a) The front-tracking point is on a horizontal grid line.
b) The front-tracking point is on a vertical grid line
. stationary grid point
x front-tracking point
edge segment belonging to the degenerate grid block
edge segment belonging to a neighbouring grid block
grid line

FIGURE 4.9. The 4 edge segments of a typical degenerate grid block associated with a front-tracking point. These diagrams provide more detailed descriptions of areas B and C in figure 4.7.

which the front-tracking point is the "centre". If the front-tracking point is on a horizontal grid line, then the degenerate grid block may be regarded as a special case of the grid block in figure 4.8: it may be regarded as a grid block in which the horizontal edge segments have shrunk to zero length; this is illustrated by figure 4.9a. Similarly, if the front-tracking point is on a vertical grid line, then the degenerate grid block may be regarded as a grid block in which the vertical edge segments have shrunk to zero length; this is illustrated by figure 4.9b. Note that the numbering scheme for the edge segments of the two degenerate grid blocks in figure 4.9 is consistent with the numbering scheme for the edge segments of the grid block in figure 4.8.

The finite-difference approximations for the matching conditions at the m-th front-tracking point are derived using a block-balance approach in which the block is taken to be the area swept out by the steam front in the vicinity of the m-th front-tracking point during the time step. A precise definition of this block is implicitly contained in the next section. The equations are analogous to equations (4.07), with A^n_{ij} replaced with A^n_m, the area of the swept-out block, and b^n_{ij} replaced with b^n_m, the boundary of the swept-out block. However, there are some differences.

One difference is that the boundary of the area swept out by the steam front during the entirety of the time step is approximated by the boundary of the area swept out during the last infinitesimal portion of the time step. (This approximation is entirely consistent with the overall methodology of the implicit-in-time finite-difference approximation.) The area swept out during the last infinitesimal portion of the time step may be identified with the degenerate grid block corresponding to the m-th front-tracking point. Thus, the boundary flow integral of equation (4.08) can be expressed as the sum of four integrals, one for each of the front edge segments touching the m-th front-tracking point.

Another difference is the approximations for the second and third terms of equations (4.09). Instead of approximations (4.10) and (4.11), the following analogous approximation is used

$$\begin{aligned}
&\iint_{A_m^n} (\phi S_p \rho_p w_c)^n \, dx \, dy - \iint_{A_m^n} (\phi S_p \rho_p w_c)^{n-1} \, dx \, dy \\
&\approx \sum_{i,j,k,l} \delta A_{ijkl}^n [(\phi S_p \rho_p w_c)_{ij}^n - (\phi S_p \rho_p w_c)_{ij}^{n-1}] \\
&- \sum_{i,j,k,l} \delta A_{ijkl}^n [(\phi S_p \rho_p w_c)_m^{n-1} - (\phi S_p \rho_p w_c)_{ij}^{n-1}] \\
&= \sum_{i,j,k,l} \delta A_{ijkl}^n [(\phi S_p \rho_p w_c)_{ij}^n - (\phi S_p \rho_p w_c)_m^{n-1}] \qquad (4.12)
\end{aligned}$$

where the summation i,j,k,l is over all area transfers associated with the m-th front-tracking point, and the subscript m in the right side refers to the downstream side of the steam front.

When these approximations are made, the partial differential equations are replaced with a set of difference equations, which may be solved numerically for the values of the locations of the front points, and for the values of the pressures, temperatures, saturations, and compositions at the stationary grid points and at the front-tracking points.

If no front-tracking points are used and the stationary grid points form a regular rectangular array ($\Delta X_i = \Delta X_{i+1}$, $\Delta Y_j = \Delta Y_{j+1}$), then the block-balance method yields the same set of algebraic equations as one of the standard finite-difference methods.

4.5 The Area Transfer Calculations

The terms of equation (4.11) which contain a δA_{ijkl}^n factor may be interpreted as transfers of the material and enthalpy contained within certain small regions, from one grid block to a neighbouring block. Analogously, the δA_{ijkl}^n fac-

tor, by itself, may be interpreted as a transfer of area from grid block k,l to grid block i,j. These δA^n_{ijkl} factors cannot be calculated as the difference between the areas of a grid block at two different time levels because a grid block might transfer areas to, or receive areas from, more than one grid block during a single time step. Instead, a more elaborate procedure for calculating the area transfer factors, δA^n_{ijkl}, is required.

This section describes the procedure for calculating the area transfer factors for the case, encountered in many time steps, in which the steam front does not sweep over any of the stationary grid points during the time step. (If the steam front does sweep over at least one of the stationary grid points, then the procedure for calculating the area transfer factors will be more complicated. A procedure for doing this has been only partially developed, and is not presented in this report.)

It is convenient to introduce the concept of "*dual grid blocks*" in order to facilitate the calculation of the area transfer factors δA^n_{ijkl}. The dual grid blocks are defined as the rectangles into which the grid lines divide the domain. In contrast with the primal grid blocks (i.e. the ones described in section 4.2), which each contain one stationary grid point located at or near the middle of the grid block (unless the grid block is at the boundary of the region), the dual grid blocks each contain four stationary grid points, one located at each of its corners. If a dual grid block contains front-tracking grid points, these also are located on its boundary. Furthermore, in contrast with the primal grid blocks, which may be irregularly shaped, all dual grid blocks are rectangles. Note that the area transfers occur between primal grid blocks: the dual grid blocks are merely a device to assist in the calculation of the area transfer factors. Outside this section (section 4.5), the term "grid block" always means "primal grid block".

There is a natural way of expressing the area transfer factors as sums of con-

tributions from each of one or more dual grid blocks. Therefore, it is possible to examine the dual grid blocks one by one, make a list of the contributions each dual grid block makes to the various area transfer factors, and then consolidate the lists by adding together all the contributions which pertain to the same area transfer factor. (Because of the role of the area transfer factors, δA^n_{ijkl}, in equations (4.11) and (4.12), the step in which the lists of contributions are consolidated is not necessary, and has been omitted from the simulator.)

There is a convenient, systematic way of enumerating all the dual grid blocks which make a contribution to at least one area transfer factor. This method exploits the fact that the front-tracking points have been numbered consecutively so that the steam front is represented by the line segments joining point #1 with point #2, point #2 with point #3, etc. Therefore, for each m between 2 and N_F (the number of front-tracking points) inclusive, the line segment joining point m−1 with point m represents part of the steam front, and slices exactly one dual grid block into two regions. It slices the same dual grid block at the end of the time step as it does at the beginning of the time step (since the steam front does not sweep over any stationary grid point during the time step). The contributions of this dual grid block to the area transfer factors may be calculated, and added to the list of contributions. Conversely, no dual grid block makes a nonzero contribution to any area transfer factor unless it is sliced by at least part of the steam front. (The apparent exception to this rule, namely transfers among regions 3A, 4B, 5A, and 5B in figure 4.12, is dealt with by counting these transfers as contributions made by the dual grid block, in figure 4.12, which contains P, and not as contributions made by the dual grid blocks which really contain regions 3A, 4B, 5A, and 5B.

Since it has been assumed that the steam front is never so contorted that it passes twice through the same dual grid block, it follows that any dual grid block

which is sliced by part of the steam front is sliced by exactly one of the N_F-1 line segments of the steam front. There are basically two possibilities for how the line segment joining front-tracking points m-1 and m slices the dual grid block: Either it passes from one side of the dual grid block to the opposite side, or it passes from one side of the dual grid block to an adjacent side.

The Opposite Side Case

The case in which the line segment passes from one side of the dual grid block to the opposite side is simpler. Let us assume without loss of generality that these two sides are vertical. Then, the simulator calculates the areas of the four regions shown in figure 4.11 and compares them with the areas calculated in the previous time step. (The extra vertical line segment in figure 4.11 bisects the dual grid block.) Clearly, if area #1 has increased during the time step, then area #2 has decreased by the same amount, and vice versa. If area #1 has increased, then the increase is counted as a contribution to $\delta A_{i,j,i,j+1}$. If area #2 has increased, then the increase is counted as a contribution to $\delta A_{i,j+1,i,j}$. Likewise, if area #3 has increased during the time step, then area #4 has decreased by the same amount, and vice versa. If area #3 has increased, then the increase is counted as a contribution to $\delta A_{i+1,j,i+1,j+1}$. If area #4 has increased, then the increase is counted as a contribution to $\delta A_{i+1,j+1,i+1,j}$.

The Adjacent Side Case

The other case is the one in which the line segment passes from one side of the dual grid block to one of the adjacent sides, thus cutting off a corner from the rest of the dual grid block. Let us assume without loss of generality that the bottom-east corner is the corner which is cut off. Then, the simulator calculates the areas of the five regions shown in figure 4.12.

In figure 4.12, point P bisects the line segment joining front-tracking grid

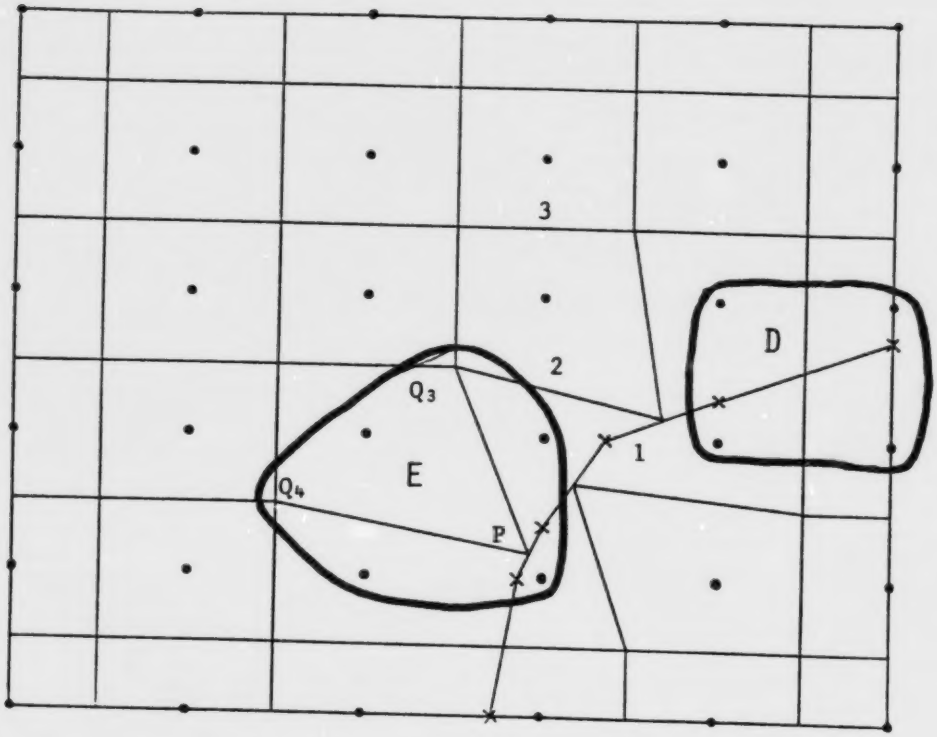

. stationary grid point

x front-tracking point

FIGURE 4.10. The context for figure 4.11 and 4.12, and for section 4.2.5. The grid blocks are the same as in figure 4.6.

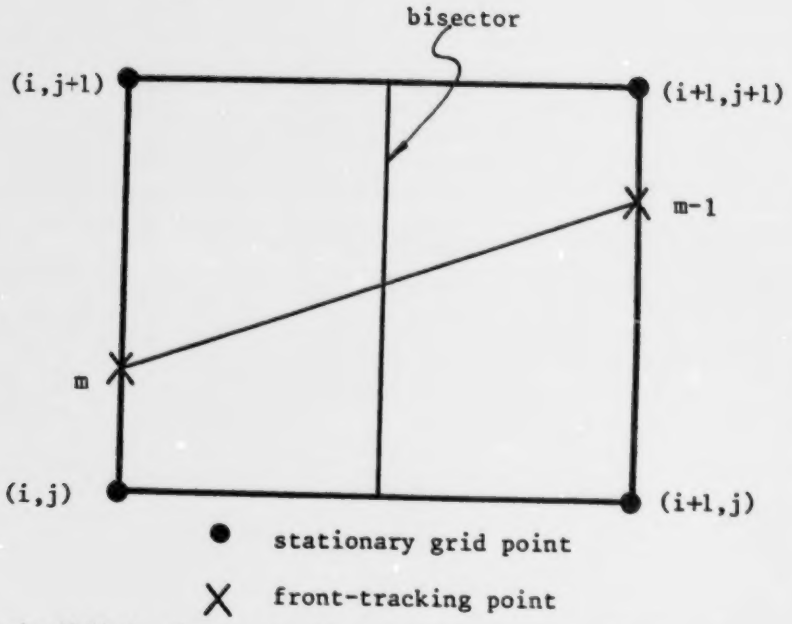

FIGURE 4.11. A typical dual grid block - the opposite-side case. This diagram provides a more detailed descriptions of area D in figure 4.10.

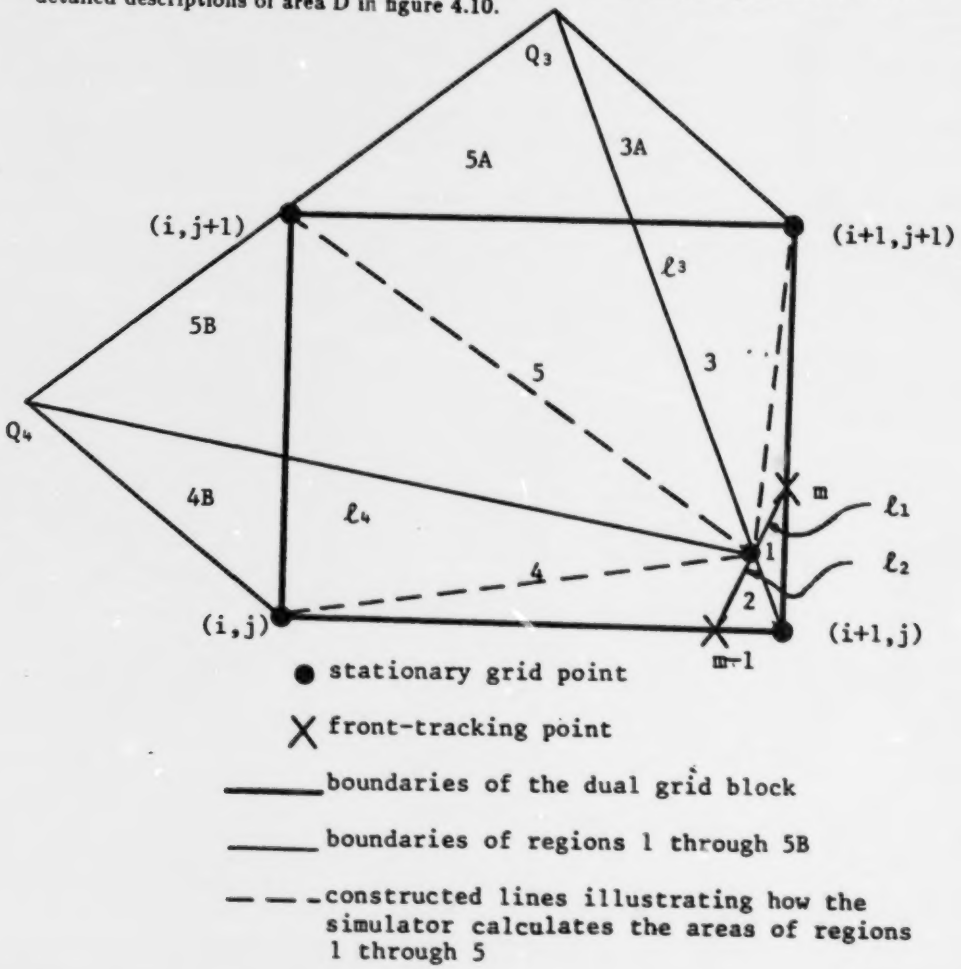

FIGURE 4.12. A typical dual grid block - the adjacent-side case. This diagram provides a more detailed description of area E in figure 4.10.

points m-1 and m. Line segments l_1, l_2, l_3, and l_4 are boundaries of primal grid blocks. The points Q_3 and Q_4 are the top-east and bottom-west corners of the primal grid block whose boundaries include both l_3 and l_4. The dotted line segments indicate the triangles which the simulator uses in order to calculate the areas.

Depending on the location of the steam front outside the dual grid block shown in figure 4.12, regions 3, 4, and 5 may, under some circumstances, include portions of the neighbouring dual grid blocks. Regions 3 and 5 include regions 3A and 5A, respectively, if and only if the steam front does not curve around and pass through the neighbouring dual grid block which contains regions 3A and 5A. Likewise, regions 4 and 5 include regions 4B and 5B, respectively, if and only if the steam front does not curve around and pass through the neighbouring dual grid block which contains regions 4B and 5B.

After calculating the areas of the five regions shown in figure 4.12, the simulator calculates the area transfers. The area transfers between diagonally opposite primal grid blocks, e.g. $\delta A_{i,j,i+1,j+1}$ are neglected: only the area transfers between directly adjacent primal grid blocks are calculated.

If area #1 has increased during the time step, then the increase is counted as a contribution to $\delta A_{i+1,j,i+1,j+1}$. On the other hand, if area #1 has decreased during the time step, then the absolute value of the decrease is counted as a contribution to $\delta A_{i+1,j+1,i+1,j}$. Likewise, if area #2 has increased during the time step, then the increase is counted as a contribution to $\delta A_{i+1,j,i,j}$. If area #2 has decreased during the time step, then the absolute value of the decrease is counted as a contribution to $\delta A_{i,j,i+1,j}$.

Area #3 can increase at the expense of either area #1 or area #5. However, increases in the *sum* of areas #1 and #3 are primarily at the expense of area #5. Therefore, if this sum has increased during the time step, then the increase is

counted as a contribution to $\delta A_{i+1,j+1,i,j+1}$. On the other hand, if this sum has decreased during the time step, then the absolute value of this decrease is counted as a contribution to $\delta A_{i,j+1,i+1,j+1}$. Likewise, if the sum of areas #2 and #4 has increased during the time step, then the increase is counted as a contribution to $\delta A_{i,j,i,j+1}$. If this sum has decreased during the time step, then the absolute value of the decrease is counted as a contribution to $\delta A_{i,j+1,i,j}$.

It has been found that it is more convenient (although computationally slightly less efficient) to apply the list of area transfer contributions directly to equations (4.11) and (4.12), than to add together the contributions to each area transfer factor and then substitute them into equations (4.11) and (4.12).

4.6 The Flow Integrals

This section describes the procedure which was used to approximate the flow integrals on the right sides of equations (4.03) and (4.04). As was discussed in the previous sections, whenever the region to which equations (4.03) and (4.04) refer is a grid block, the flow integrals on the right sides of these two equations can be written as the sum of eight integrals, one over each edge segment of the grid block, as shown in figure 4.8. Likewise, whenever the region to which equations (4.03) and (4.04) refer is the area swept out by the steam front in the vicinity of a front-tracking grid point, the flow integrals on the right sides of equations (4.03) and (4.04) can be written as the sum of four integrals, one over each front edge segment touching the front-tracking point, as shown in figure 4.9. Thus, the problem of approximating the flow integrals on the right sides of equations (4.03) and (4.04) reduces to the problem of approximating the flow integrals over an arbitrary edge segment.

Several cases must be considered:

Null Edge Segments:

If a grid block is on the boundary of the simulation domain, then some of its corners coincide, and it has fewer than eight "real" edge segments (length greater than zero). However, it is convenient to consider such grid blocks to still have eight edge segments, some of which are "null" edge segments, with zero length. Likewise, if a front-tracking point is on the boundary of the solution domain, it is convenient to define four edge segments for the front-tracking point, although two of these edge segments are "null" edge segments with zero length. In either case, if an edge segment is a null edge segment, then all flow integrals equal zero.

Boundary Edge Segments:

If a grid block is on the boundary of the simulation domain, then at least two (and sometimes four) of its edge segments lie on the boundary of the solution domain. It is natural to refer to these edge segments as "boundary edge segments". For the purposes of this calculation, it is expedient to combine the integrals over all boundary edge segments belonging to the same grid block, even if the grid block is a corner block (i.e. a grid block located at one of the four corners of the simulation domain). The flow integrals may be approximated (all integrals are taken over the union of the boundary edge segments) as

$$\begin{aligned} \int -\tau_p w_c \underline{\nabla}\Phi_p \cdot \underline{n}\, ds &\approx (\tau_p w_c)_{i,j} \int -\underline{\nabla}\Phi_p \cdot \underline{n}\, ds \\ &= \left(\rho_p w_c \frac{\lambda_p}{\sum \lambda_p} \right)_{i,j} (\sum \lambda_p)_{i,j} \int -\underline{\nabla}\Phi_p \cdot \underline{n}\, ds \end{aligned} \tag{4.13}$$

$$\begin{aligned} \int -\sum_p \tau_p h_p \underline{\nabla}\Phi_p \cdot \underline{n}\, ds &\approx (\sum_p \tau_p h_p)_{i,j} \int -\underline{\nabla}\Phi_p \cdot \underline{n}\, ds \\ &= \left(\sum_p \rho_p h_p \frac{\lambda_p}{\sum \lambda_p} \right)_{i,j} (\sum \lambda_p)_{i,j} \int -\underline{\nabla}\Phi_p \cdot \underline{n}\, ds \end{aligned} \tag{4.14}$$

(the subscripts i,j refer to the one grid block to which the boundary edge segment belongs) unless the boundary conditions include specified injection rate ratios. If

these injection rate ratios are specified volumetrically, then equations (4.13) and (4.14) should be modified by replacing the mobility ratios with injection rate ratios. If the injection rate ratios are specified on a molar or mass basis, the required modification of (4.13) and (4.14) is also straight-forward.

In equations (4.13) and (4.14), all the flow integrals are expressed in terms of a single quantity,

$$(\sum \lambda_p)_{i,j} \int -\underline{\nabla} \Phi_p \cdot \underline{n} \, ds$$

i.e. the total volumetric flow rate. This quantity is specified if a specified-flow-rate boundary condition is used, but is treated as a primary unknown, in the place of pressure, if a specified-pressure boundary condition is imposed.

Once the flow integral over the two (or four) boundary edge segments is computed, it is prorated over the two (or four) edge segments according to their length, whether or not the grid block is a corner block. If the boundary edge segments do not belong to a corner block, then this prorating introduces no discretization error because whenever the two flow integrals are used, they are added together. If the boundary edge segments do belong to a corner block, then this prorating may introduce discretization errors if the boundary conditions change sharply at the corner. If we decide to use such boundary conditions, and if we decide that the resulting discretization error is unacceptable, it is possible to modify the simulator so that this discretization error is eliminated.

Interior Edge Segments

The term "interior edge segments" refers to all edge segments which are neither null edge segments, nor boundary edge segments. The flow integrals over the interior edge segments may be approximated as

$$\int -\tau_p w_c \underline{\nabla} \Phi_p \cdot \underline{n} \, ds \approx (\tau_p w_c)_{i,j} \int -\underline{\nabla} \Phi_p \cdot \underline{n} \, ds \qquad (4.15)$$

and

$$\int -\sum_p \tau_p h_p \underline{\nabla}\Phi_p \cdot \underline{n}\, ds \approx (\sum_p \tau_p h_p)_{i,j} \int -\underline{\nabla}\Phi_p \cdot \underline{n}\, ds \tag{4.16}$$

Upstream weighting is used for $(\tau_p w_c)_{i,j}$ and $(\sum_p \tau_p h_p)_{i,j}$ with one exception: if the upstream point is a front-tracking point and the downstream point is in the steam zone, then downstream weighting is used. This exceptional case occurs infrequently, but is necessary in order that, should the front reverse its direction of movement, it be allowed to move.

The original approximations which were derived for the integral $\int -\underline{\nabla}\Phi_p \cdot \underline{n}\, ds$ are more elaborate (higher order) then those presented in the main body of the report. However, when the higher order approximations were used, it was found that they induced severe spatial oscillations in the pressure, in the region adjacent to the steam zone. Therefore, they were replaced with simpler lower order approximations: some accuracy was sacrificed, but significant stability with respect to spatial oscillations was gained. The original more elaborate representation is given in the appendix.

Whereas these more elaborate approximations involved the pressures at four grid points (moving and/or stationary), the simplified approximations contain the pressures at only two grid points.

In the following, a distinction is made between front edge segments (i.e., the edge segments which together constitute an approximate description of the steam front, e.g. edge segment #1 in figure 4.10) and edge segments which are not front edge segments, e.g. edge segments #2 and #3 in figure 4.10.

If the interior edge segment is not a front edge segment, then the two grid points used in the simplified approximation are the grid points belonging to the two grid blocks beside the interior edge segment. If the interior edge segment *is* a

front edge segment, then the two grid points used in the simplified approximation are the front-tracking point which is at the end of the front edge segment, and the grid point belonging to the one grid block beside the front edge segment.

Why there is only one grid block beside each front edge segment requires a little explanation. Since the various flow rates might be discontinous at the steam front, it is convenient to consider the steam front as consisting of pairs of front edge segments located side-by-side, as shown in figure 4.9. Therefore, there is only one grid block beside each member of a pair of front edge segments.

Note that in either case, the two grid points either have the same X-coordinates, or have the same Y-coordinates.

Now that the two grid points used in the simplified approximation have been defined, the following paragraphs explain how they are used.

An inspection of figure 4.10 shows that every edge segment may be classified as either mainly horizontal or mainly vertical, even if it has both horizontal and vertical components. If the interior edge segment is a horizontal edge segment, then the approximation

$$\int -\underline{\nabla}\Phi_p \cdot \underline{n}\, ds \approx \int -\frac{\partial \Phi_p}{\partial Y}\, dX$$

is used. Whether or not the interior edge segment is a front edge segment, the two grid points have the same X-coordinate (but different Y-coordinates). Therefore, the partial derivative $\partial \Phi_p / \partial Y$ may be approximated by the constant

$$\frac{\partial \Phi_p}{\partial Y} \approx \frac{\Phi_{p2} - \Phi_{p1}}{Y_2 - Y_1}$$

where Y_1, Y_2, Φ_{p1}, and Φ_{p2} are the Y-coordinates and values of Φ_p at the two grid points (as defined above) used in the approximation. Combining these two approximations, we derive

$$\int -\underline{\nabla}\Phi_p \cdot \underline{n}\, ds \approx \left(\frac{\Phi_{p2}-\Phi_{p1}}{Y_2-Y_1}\right) \times |\, X_B - X_A\,| \tag{4.17}$$

where X_A and X_B are the X-coordinates of the endpoints of the interior edge segment.

Likewise, if the interior edge segment is a vertical edge segment, then the approximations

$$\begin{aligned} \int -\underline{\nabla}\Phi_p \cdot \underline{n}\, ds &\approx \int -\frac{\partial \Phi_p}{\partial X}\, dY \\ &\approx \left(\frac{\Phi_{p2}-\Phi_{p1}}{X_2-X_1}\right) \times |\, Y_B - Y_A\,| \end{aligned} \tag{4.18}$$

are used. Here X_1 and X_2 are the X-coordinates of the two grid points (as defined above) used in the approximation. (they have the same Y-coordinate), and Y_A and Y_B are the Y-coordinates of the endpoints of the (vertical) interior edge segment.

If there are no front-tracking points in the grid , then all the grid blocks are rectangular, and these approximations reduce to the standard 5-point finite-difference approximations.

4.7 The Solution Method

After all the substitutions described above have been inserted into the system of equations (4.07), the result is a system of non-linear algebraic equations

$$\underline{F}(\underline{U}) = \underline{0} \tag{4.19}$$

where $\underline{U}$ is a vector consisting of a set of discrete pressures, temperatures, saturations, mole fractions, boundary flow rates, and steam front locations.

This system is solved using the Newton-Raphson iteration method

$$\underline{U}^{(k+1)} = \underline{U}^{(k)} - [\underline{J}^{(k)}]^{-1}\, \underline{F}(\underline{U}^{(k)}) \tag{4.20}$$

where $\underline{\underline{J}}^{(k)}$ is the Jacobian $(\partial \underline{F}/\partial \underline{U}^T)$ evaluated using $\underline{U}^{(k)}$. The iteration procedure is continued until an iteration step occurs, in which either no component of $\underline{U}$ changes by more than a pre-determined amount, or a sign of trouble is detected.

Both the equations and the variables are divided into groups such that each group contains the equations/variables pertaining to a particular grid point.

The variables pertaining to each grid point depend on the type of grid point. This dependence is shown in table 4.1.

TABLE 4.1. The variables in $\underline{U}$ which pertain to a given grid point.

grid point type #	Variable #1	Variable #2	Variable #3	Variable #4	Variable #5
1	S_w	x_1	x_2	P	T
2	S_w	x_1	x_2	q_F	T
3	S_w	x_1	x_2	P	S_g
4	S_w	x_1	x_2	q_F	S_g
5	S_w	x_1	x_2	P	front location

grid point type #

1 - no vapour phase present: an interior grid block, or a boundary grid block with specified flow-rate

2 - no vapour phase present: a boundary grid block with specified pressure

3 - a vapour phase is present: an interior grid block, or a boundary grid block with specified flow-rate

4 - a vapour phase is present: a boundary grid block with specified pressure

5 - a front-tracking grid point

The equations of $\underline{F}$ which pertain to each grid point are as follows: Equation #1 is the sum of the balances for liquid water and steam. Equation #2 is the sum of the balances for the volatile hydrocarbon component #1 in the liquid hydrocarbon phase and in the vapour phase. Equation #3 is the same as equa-

tion #2 except that the balances are for the volatile hydrocarbon component #2.

The obvious choices for equations #4 and #5 are the balance for the heavy non-volatile hydrocarbon component, and the overall enthalpy balance. However, it was observed that the simulator did not work properly if these two balances were used because the Jacobian was very ill-conditioned. It was thought that the Jacobian would be better conditioned if equations #4 and #5 were replaced with linear combinations of all the balances chosen so that certain saturation and composition derivatives would cancel. Thus, equation #4 was chosen to be a linear combination of the material balances, namely the sum of equation #1 divided by the liquid water molar density, equation #2 divided by the molar density of the volatile hydrocarbon component #1 in the liquid phase, equation #3 divided by the molar density of the volatile hydrocarbon component #2 in the liquid phase, and the balance for the heavy non-volatile hydrocarbon component divided by the molar density of this component (in the liquid phase). This linear combination can be interpreted as a volume balance in the region where there is no steam.

The idea of constructing linear combinations of these balances in order to eliminate saturation derivatives is an important part of the IMPES[1] (IMplicit-Pressure-Explicit-Saturation) method of reservoir simulation. However, whereas the IMPES linear combinations are chosen to eliminate as many of the δ(saturation)/δ(time) difference terms as possible, even at the expense of retaining the condensation terms, our linear combination eliminates fewer δ(saturation)/δ(time) difference terms, but eliminates all the condensation terms.

Likewise, equation #5 was chosen to be the difference between the overall enthalpy balance and the following sum: the sum of equation #1 multiplied by the liquid water molar enthalpy, equation #2 multiplied by the molar enthalpy of the volatile component #1 in the liquid phase, equation #3 multiplied by the molar enthalpy of the volatile component #2 in the liquid phase, and the balance

for the heavy non-volatile component multiplied by the molar enthalpy of this component (in the liquid phase). This linear combination is similar to the linear combination used by Shutler[2] and by Beattie[3] to derive sequential algorithms for reservoir simulation. However, Shutler and Beattie both multiply the vapour-phase material balances by vapour-phase enthalpies, thus introducing condensation terms into the linear combination, whereas we multiply the vapour-phase material balances by liquid-phase enthalpies, thus eliminating the condensation terms.

Up to this point, only a very cursory comparison of the effectiveness of the two choices for equation #4 and for equation #5 has been made. Therefore, the simulator contains a pair of options whereby either candidate for equation #4 can be selected, and either candidate for equation #5 can be selected.

4.8 References for Chapter 4

1. e.g. K. Aziz and A. Settari, "*Petroleum Reservoir Simulation*", (Applied Science Publishers, London, 1979), section 5.3.

2. N.D. Shutler, "Numerical, Three-Phase Simulation of the Linear Steamflood Process", *Society of Petroleum Engineers Journal* **9**, 232-246 (1969).

3. C.I. Beattie, "*Numerical Simulation of Oil Recovery by Steam Injection*", M.A.Sc. Thesis. University of Toronto, 1980.

5. A SURVEY OF REPORTED PHYSICAL PROPERTIES FOR THE COLD LAKE RESERVOIR

5.1 Introduction

There is surprisingly little information in the literature concerning the physical properties of the Cold Lake bitumen deposits. Indeed, semi-comprehensive tabulations of the Cold Lake physical properties listed in this report could be found in only five references[8,14a,23,25,35], one of which[23] has several obvious errors, and probably has some less obvious errors as well. The other references cited in this section of the report belong to one of three sets. One set contains references which claim to describe the Cold Lake reservoir, but which collectively list only a handful of the properties of interest for reservoir simulations. For example, many of the references in this set give a value for absolute permeability, but none give any relative permeability data. Many of these references give a value for the density of bitumen, but almost none describe how the density varies with temperature or pressure. Many of these references show how the viscosity of the bitumen varies with temperature, but none describe how the viscosity varies with the amount of methane dissolved. Some of these references describe the composition of the bitumen, and a few give volatility data, but none give enough information to allow one to construct a useful description of the bitumen as a mixture of two or more pseudocomponents.

The second set (which is rather small) contains references[13,17,33,34,40] which describe in detail a few of the physical properties. However, many of the physical properties of interest are not mentioned by any of the references in this set.

The third set (which is also small) contains references[41–45] which do not describe any of the physical properties of the Cold Lake reservoir. Instead, they describe the physical properties of a different reservoir, and thus give a rough guide for the corresponding physical properties of the Cold Lake reservoir.

It is likely that several organizations have unpublished collections of data on Cold Lake physical properties, and that these collections are more detailed and more accurate than what we have been able to obtain from the published literature. It would be beneficial to gain access to some of this unpublished information.

All quantities have the standard SI units.

5.2 Initial Reservoir Conditions

Many publications contain values for the initial temperature, pressure, and hydrocarbon saturation. These are given in table 5.1. The discrepancies in the published values may be attributed to heterogeneity in the Cold Lake reservoir, to the hydrostatic vertical pressure gradient, and to different definitions of saturation. We selected representative values for the temperature and hydrocarbon saturation from the paper by Reddy et al.[39], since it describes the Cold Lake reservoir in considerable detail. The values of initial reservoir pressure given by Finbow and Koop[9] are the most useful since they give pressure as a function of vertical distance, whereas most publications give only a single representative pressure. While most authors do not mention any vapour phase, three publications suggest that a small amount of vapour may be present. It should be recognized, however, that the accurate measurement of the vapour phase saturation is very difficult due to the disruption of core samples that accompanies decompression as they are brought to surface conditions[45].

With respect to composition of the in situ oil, some distillation curve data are available as indicated in table 5.1. These distillation data can be used to define pseudocomponents for the oil. However, for the purposes of most steam injection simulations, it is sufficient to treat the bitumen as only a two-component mixture of heavy oil and methane. Methane gas-oil ratios of 9.8 m^3/m^3 were

TABLE 5.1. A survey of commonly reported reservoir properties - Part 1.

Ref.	Year	Formation	Temperature	Pressure	Hydrocarbon Saturation	Molecular Weight	Distillation data?
1	1973	Clearwater			0.58		
4	1974	Mannville C	55°F.	440 psi(g?)	0.55?		sat. methane at 455 psia
5	1974		55°F.	450 psi	0.55		
6	1974/5	Mannville	55°F.	440 psi	0.55?		
7	1975	Cummings	55°F.	400 psi?	0.65		
8	1976		55°F.	440 psia 115 ft. below top	0.65		
9	1977	Mannville C	15.6°C.	function of depth 2500-3200kPa	0.38-0.58		
10	1977				0.09-0.10(wt.)		
13	1977					490	
14	1974/7		55°F.	450 psi	0.515-0.55		initial GOR: 41.5 scf/STB
15	1978	Clearwater	55°F.	440 psi	0.55		
16	1979	Clearwater	13°C. (55°F.)	3100 kPa (450 psig)			initial GOR: 9.8 m^3 (st)/m^3 (55 SCF/bbl)
18	1979		55°F.	450 psi	0.60		
19	1979						initial GOR: 35 scf/bbl (6.23 m^3/m^3)
22	1981		15°C.?	2500 kPa	0.42		Yes
23	1981	Marguerite Lake	16°C.	400 psi (2758 kPa)	0.67	702	pseudo-components
24	1981	Clearwater			0.14-0.16(wt.)		
25	1981		65°F.	473 psia			
26	1981						Yes

TABLE 5.1. A survey of commonly reported reservoir properties - Part 1 (cont.).

Ref.	Year	Formation	Temperature	Pressure	Hydrocarbon Saturation	Molecular Weight	Distillation data?
27	1981	Grand Rapids			0.76		
27	1981	Clearwater	55°F.	440 psig	0.73	490	Yes
27	1981	McMurray	50°F.		0.69		
29	1982	Clearwater	55°F.	440 psig	0.73	490	Yes
29	1982	Marguerite Lake	15°C. (59°F.)	2700 kPa (392 psi)			
30	1982	Clearwater	55-62°F.			490	
31	1983	Grand Rapids			0.76		
31	1983	Clearwater	15°C.	3030 kPa	0.73	490	Yes
31	1983	McMurray	10°C.		0.69		
32	1983		13°C.	3100 kPa	0.70		initial GOR: 9.8 $m^3(ST)/m^3$
35	1984	Beaver Crossing	60.0°F.	400 psia	0.77		
36	1984	Clearwater?	-20°C.				
38	1984					500.4	
39	1984	Grand Rapids	13-21°C.		0.65-0.82		
39	1984	Clearwater	13-21°C.		0.64-0.65		
39	1984	Wabiskaw/ McMurray	14-26°C.		0.7-0.85		
40	1984	Lower Grand Rapids				568	Yes

TABLE 5.1. A survey of commonly reported reservoir properties - Part 2.

Ref.	Formation	Porosity	Permeability	Density	$\mu_{initial}$	μ_{other}
1	Clearwater	0.395				
2	Upper Mannville	0.28-0.43 0.37 (avg.)	300-1300 mD up to 3000 mD	1000-986 kg/m^3 10-12° API		
3				10-12° API		4000-100,000 cp at 100° F.
4	Mannville C	0.37	≤3000 mD	10-12° API	100,000 cp	graph
5		0.35	~1 D	10° API	100,000 cp	
6	Mannville	0.37	3000 mD	10-12° API	100,000 cp	graph
7	Cummings	0.36	4-14 D	10.5° API	~10^5 cp	graph?
8		0.36	k_h : 8000 mD k_v : 800 mD	62.14 lb./cu. ft.	100,000 cp	tabulated
9	Mannville C	0.30	k_h : 0-2.467×10^{-12} m^2 k_v : 0-0.247×10^{-12} m^2			
10		0.30-0.35				same graph as in Winestock [4]
11		0.35-0.45				
12		0.30-0.35		10-12° API		graph
14		0.285-0.385	795-1240 mD	62.3 lb./cu. ft.	100,000 cp	
15	Clearwater	0.37	≤3000 mD	10-12° API	100,000 cp	same graph as in Winestock [4]
16	Clearwater	0.35	1.5 D	10.3° API (998 kg/m^3 @15° C.)	100,000 cp	graph similar to the one in Winestock [4]
17						for 27.5-72.5° C. for various shear rates
18		0.35	1500 mD	10° API	100,000 cp	
20						graph
21		0.37 @138 kPa	2.86 μm^2	999.6 kg/m^3 @138 kPa, 23.9° C.	1.2×10^3 Pa.s @23.9° C.	table up to 260° C.
22		0.30	>1 μm^2	988 kg/m^3		17,600 mPa.s @21° C. 3,300 mPa.s @38° C. 650 mPa.s @60° C.
23	Marguerite Lake	0.21-0.31	0.55-1.70D	1.41×10^3 mol/m^3		formula
24	Clearwater	0.18-0.35				
25		0.3	500 mD	62 lbm./cu. ft.	200,000 cp	table
26				992 kgm/m^3		160 mPa.s @100° C.

TABLE 5.1. A survey of commonly reported reservoir properties - Part 2 (cont.).

Ref.	Formation	Porosity	Permeability	Density	$\mu_{initial}$	μ_{other}
27	Grand Rapids	0.34-0.40				
27	Clearwater	0.34-0.40?	≤3 D	10-12° API	100,000 cp	100 cp @212° F.
27	McMurray	0.38-0.46				
28		0.37	3000 mD	0.990-1.000 g/cm^3		100 cP (u.r.c.)
29	Clearwater	0.34-0.40	≤3000 mD	10-12° API	100,000 cp	100 cp @212° F.
29	Marguerite Lake	0.30				6800 mPa.s @38° C. 680 mPa.s @66° C. 130 mPa.s @96° C.
30	Clearwater			9.5° API 1.004 g/mL	1×10^5 cp	
31	Grand Rapids	0.34-0.40				
31	Clearwater	0.38-0.46	≤300 μm^2 [sic]	10-12° API (0.986-1.00)	100 Pa.s @15° C.	0.1 Pa.s @100° C.
31	McMurray	0.30-0.36				
32		0.35	1.5 D	10.2° API 0.9987	100 Pa.s	8×10^{-3} Pa.s @200° C.
33				for 20-90° C. e.g. 990 kg/m^3 @20° C.	400,000 mPa.s @21.1° C.	for 21.1-104.0° C. for various shear rates e.g. 60 mPa.s @104.0° C.
34				10.2° API		
35	Beaver Crossing	0.38	2500 mD	62.4 lbm/ft^2	200,000 cp	2.5 cp @600° F.
36	Clearwater?	0.30-0.32	>1 D	9-12° API	3000-10,000 poise	
37						graph same as in Buckles [16]
39	Grand Rapids	0.28-0.35	1-4 D	985-1001 kg/m^3	0.5-1×10^6 mPa.s	
39	Clearwater	0.275-0.35	0.5-3 D	986-1000 kg/m^3	10^5 mPa.s	
39	Wabiskaw/ McMurray	0.32-0.33	1.5 D	994-1000 kg/m^3	10^4-10^6 mPa.s	
40	Lower Grand Rapids			10.2° API		44,500 cp @25° C. 13,800 cp @35° C.

reported by Buckles[16] of Esso Resources Canada, and also by Mainland and Lo[32]. Lower values of 7.5 and 6.3 m^3/m^3 were reported by Weinstein et al.[14] and Farouq-Ali[19] respectively. Once again, some degree of variability is to be expected. Indeed, it is this variation in GOR which probably results in a significant part of the observed variation in reservoir pressure as reported in the literature.

Reasonably representative values of the initial conditions are

Temperature:	$14^{o}C.$
Pressure (at bottom):	3180 kPa
Vertical Pressure Gradient:	-9.8 kPa/m
Bitumen Saturation:	0.64
Vapour Saturation:	0.001
Gas-Bitumen Ratio:	9.8 m^3/m^3
	0.71% (wt.)

5.3 Reservoir Matrix Properties

In this section, we summarize the information concerning the reservoir properties which affect fluid-solid interactions.

5.3.1 Porosity

A summary of published values is given in table 5.1. Although a value of 0.37 appears to be most representative of the data, Dusseault[45] pointed out that many porosity measurements are in error because no allowance was made for disturbance during coring. In a later paper, Dusseault and Van Domselaar[36] recommended an average value of 0.31. This value is corroborated by a recent detailed survey by Reddy et al.[39], who reported a range of values between 0.275 and 0.35. Hence, a value of 0.31 appears to be the most reasonable choice for porosity.

5.3.2 Absolute Permeability

Table 5.1 provides a summary of the available data. There is considerable variation in the fines content of the sand from site to site, and, even in a single site, between the top and bottom of the pay. Hence, large variations in absolute permeability are to be expected. A value of 1.5×10^{-12} m^2 seems to be most representative.

5.3.3 Relative Permeability

Four authors have published data concerning the relative permeability in Cold lake. The endpoint data are tabulated in table 5.2. Once again, even with the small amount of data available, there is considerable variation. Weinstein et al.[14a] attributed their very low values of k_{rw} and k_{rg} to the formation of emulsions as the oil and water flow through the sand. The data of Coats[8], Settari and Raisbeck[25], and Duerksen et al.[35] are relatively consistent with one another, but the data in the latter two papers are incomplete.

Duerksen et al.[35] reported a significant dependence of the irreducible water saturation $S_{w,irr}$ on reservoir temperature. Such a strong dependence may have a significant effect on recovery performance.

Taking all factors into account, we recommend the use of the data of Coats[8]. For completeness, the relative permeability tables of Coats are reproduced in table 5.3.

5.3.4 Compressibility and Thermal Properties

The compressibility and thermal properties of the formation are given in table 5.4. There seems to be considerable disagreement concerning the rock compressibility, α_{rock}. However, Dusseault and Van Domselaar[36] have investigated the effect of different core sampling procedures on the measured values of this property, and report that the correct value lies in the range

TABLE 5.2. Relative Permeability Data.

Author	Duerksen et al.[35]	Coats[8]	Weinstein et al.[14a]	Settari and Raisbeck[25]
$S_{w,irr}$ 60°F.	0.2	0.35	0.25	0.30
$S_{w,irr}$ 650°F.	0.5			
$S_{s,crit}$	0.0	0.0	0.025	--
$S_{or}(w)$	0.211	0.20	0.19	0.25
$S_{or}(g)$	0.09	?	?	--
k_{rw} at S_{or}	0.164	0.200	0.017	0.20
k_{ro} at $S_{w,irr}$	0.4	0.8	1.0	0.93
k_{rg} at s_{or}	0.18	0.2	0.023	--
absolute permeability ($10^{-12} m^2$)	2.5	8.0 (horz) 0.8 (vert)	0.8-1.2	0.5

TABLE 5.3. The relative permeability tables of Coats[8].

Water-Oil Relative-Permeability			Gas-Oil Relative-Permeability		
S_w	k_{rw}	k_{row}	$S_L=S_{wir}+S_g$	k_{rog}	k_{rg}
0.2	0	1	0.290	0.0000	0.1700
0.25	0.0102	0.7690	0.395	0.0294	0.1120
0.294	0.0168	0.7241	0.433	0.0461	0.1022
0.357	0.0275	0.6206	0.515	0.0883	0.0855
0.414	0.0424	0.5040	0.569	0.1172	0.0761
0.49	0.0665	0.3714	0.614	0.1433	0.0654
0.557	0.0970	0.3029	0.663	0.1764	0.0500
0.63	0.1148	0.1555	0.719	0.2170	0.0372
0.673	0.1259	0.0958	0.750	0.2255	0.0285
0.719	0.1381	0.0576	0.805	0.2919	0.0195
0.789	0.1636	0	0.850	0.3373	0.0121
1.0	1.0	0	0.899	0.5169	0.0026
			1.000	1.0000	0.0000

$0.2 - 0.8\times10^{-6}$/kPa. Hence, we have selected 0.5×10^{-6} as representative.

There is a general consensus that the thermal conductivity of the formation, k_f, is somewhat smaller than that for the overburden, k_{OB}. Duerksen et al.[35], however, report the opposite trend in their data. Finally, the values reported for rock and overburden heat capacity, $c_{p,r}$ and $c_{p,OB}$ are fairly consistent, except for Duerksen et al.

5.4 Bitumen Properties

5.4.1 Compressibility and Thermal Properties

The bitumen compressibility and thermal properties are given in table 5.4. The compressibility of bitumen, α_{oil}, is poorly documented by the authors cited in the table. However, Butler[46] suggests a value of $0.47\times10^{-6}\ kPa^{-1}$. There is reasonable agreement on the coefficient of thermal expansion, β_{oil}, and the heat capacity $c_{p,o}$.

5.4.2 Density

Table 5.1 provides a summary of published data for the density of the bitumen at reservoir conditions. A value of 990 kg/m^3 appears to be most representative.

A graph of the density of Cold Lake bitumen as a function of temperature is given by Steinborn and Flock[33]. Unfortunately, their graph goes no further than $90°C$. Other authors simply assume that the density varies linearly with temperature and with pressure, and publish the relevant coefficients, namely α_{oil} and β_{oil} (see the summary in table 5.4). Because of the lack of data on the nonlinear variation of density with temperature (for temperatures larger than $90°C$.) and with pressure, we recommend using these coefficients to construct the formula

$$\rho = 990 - 7\times10^{-4}(T - T_{initial}) + 0.47\times10^{-9}(P - P_{initial})$$

TABLE 5.4. Miscellaneous bitumen and formation properties.

Author **	Compressibility		Thermal Expansion	Thermal Conductivity		Heat Capacity		
	α_{rock} $\left(\frac{10^{-6}}{kPa}\right)$	α_{oil} $\left(\frac{10^{-6}}{kPa}\right)$	β_{oil} $\left(\frac{10^{-4}}{K.}\right)$	k_f $\left(\frac{W}{m \cdot K.}\right)$	k_{OB} $\left(\frac{W}{m \cdot K.}\right)$	$c_{p,o}$ $\left(\frac{kJ}{kg \cdot K.}\right)$	$c_{p,r}$ $\left(\frac{kJ}{m^3 \cdot K.}\right)$	$c_{p,OB}$ $\left(\frac{kJ}{m^3 \cdot K.}\right)$
Coats[9]	0.6	1.5	9	2.77	2.77	2.1	2300	2300
Settari et al.[35]	7	--	5.2	1.63	2.52	2.04	2300	2500
Duerksen et al.[25]	18†	0.7	7.2	2.75	1.69	2.1	1250	2120
Weinstein et al.[14a]	15	--	--	1.73	2.42	--	2300	2700
recommended value	0.5	0.47‡	7	2	2.5	2.1	2300	2400

** The values in this table were converted from the foot-pound-second system to SI. This causes small inaccuracies in the actual values, and misrepresents slightly the implied precision of the numbers.

† This figure is the compressibility of the formation, not of the rock.

‡ This value is used by Butler[46].

The density of the vapour phase may be calculated by regarding the vapour phase as an ideal solution (as defined, eg. by Denbigh[47]) of methane and steam. The density of the methane may be calculated using the ideal gas equation, and the density of the steam may be obtained from steam tables.

5.4.3 Viscosity

Table 5.1 provides a summary of published data. Although there are exceptions, the consensus is that the viscosity of the bitumen is 100 Pa.s at the initial reservoir temperature of $13^{o}C$. There is also a limited consensus regarding the viscosity as a function of temperature, as several publications[4,10,15,16,37] contain graphs, which are almost identical, and several other publications have either graphs or tabulated values, which are similar to the graph presented, e.g., by Winestock[4]. The curve on this graph may be fitted quite accurately, over the entire range of temperatures ($10–350^{o}C$.) of interest to us, by the equation

$$\log_{10}(\log_{10}(\mu_C)) = \frac{2150}{T+354} - 2.660 \qquad (5.1)$$

where μ_C is the viscosity of Cold Lake bitumen in centipoise (1 cp = 10^{-3} Pa.s), and T is the temperature in degrees Kelvin. It is interesting that the curve on the same graph for the viscosity of Athabasca bitumen can be fitted accurately by the equation

$$\log_{10}(\log_{10}(\mu_A)) = \frac{2150}{T+354} - 2.572$$

which is the same as the analogous equation for Cold Lake bitumen, except for a different constant.

It should be noted that there is considerable heterogeneity in the Cold Lake deposit, as Duerksen et al.[35], Reddy et al.[21], and Settari and Raisbeck[25] describe Cold Lake bitumens considerably more viscous than the one to which equation (5.1) applies. Nevertheless, the equation (5.1) for the viscosity of Cold Lake

bitumen as a function of temperature may be taken as representative.

No data are available describing the effect of dissolved methane on the viscosity of Cold Lake bitumen. Perhaps, viscosity-composition-temperature correlations (e.g.[41,48]) valid for other oil sands deposits or heavy oil reservoirs might be adapted in order to describe the Cold Lake bitumen.

5.4.4 Enthalpy of Solution of Methane

No data are available. However, the importance of this enthalpy change is probably small compared with the importance of the enthalpy of vaporization of water.

5.4.5 Solubility of Methane in Bitumen

As is mentioned above, a methane gas-oil ratio of 9.8 $m^3(ST)/m^3$ was reported by Buckles[16], and by Mainland and Lo[32]. Lower values of 7.5 and 6.3 $m^3(ST)/m^3$ were reported by Weinstein et al.[14] and by Farouq-Ali[19] respectively. Since it is believed (see the viscosity-temperature graph of Winestock[4]) that the bitumen is saturated with methane at initial reservoir conditions, it is reasonable to take the largest reported gas-oil ratio, namely 9.8 $m^3(ST)/m^3$ (= 0.71% wt.) as the solubility of methane in Cold Lake bitumen at 13^oC. and 3100 kPa.

Data for the solubility of methane in Cold Lake bitumen at other temperatures and pressures are not available. However, data for the solubility of methane in bitumen from other oil sands deposits are available [41–44], and may be used as a guide for estimating a tentative correlation for the Cold Lake bitumen. The data for the solubility of methane from the other oil sands deposits may be fitted to within a few percent by the following empirical correlations, which we have derived:

For Wabasca bitumen,

$$\log_{10}\left(\frac{\hat{x}_m}{P}\right) = -1.04 + \frac{110}{T} - 0.010\,P$$

where T is the temperature in degrees Kelvin, P is the pressure in MPa, and $\hat{x}_m$ is the weight-percent solubility of methane given as a percentage.

For Peace River bitumen (same units),

$$\log_{10}\left(\frac{\hat{x}_m}{P}\right) = -1.07 + \frac{120}{T} - 0.017\,P$$

For Athabasca bitumen (same units),

$$\log_{10}\left(\frac{\hat{x}_m}{P}\right) = -1.76 + \frac{270}{T}$$

(The third term was omitted because no systematic variation of $\log_{10}(\hat{x}_m/P)$ with P was observed; only scatter was observed).

The average percentage discrepancies between these correlations and the experimental values were calculated. Two of the 58 reported values were omitted because a blatant inconsistency between the reported weight-percent solubility and the reported volume-percent solubility was observed. Thus, the average percentage discrepancy is 3.8% for the Wabasca correlation, based on 12 points; 2.5% for the Peace River correlation, based on 15 points; and 8.9% for the Athabasca correlation, based on 29 points.

Mehrotra and Svrcek[41] give a 4-parameter correlation for the solubility of methane and other gases, but this correlation applies only to the Athabasca bitumen which, of the three bitumens, is the most different from Cold Lake bitumen. The average discrepancy of their correlation (for methane only) is 9.3%, based on 29 points (9.7%, based on 30 points, if the inconsistent set of values is not omitted). Thus, the discrepancy of our 3-parameter correlation (which can even be considered to be a 2-parameter correlation for the Athabasca bitumen) is slightly

better than the discrepancy of their 4-parameter correlation.

When the initial conditions of the Cold Lake reservoir (as reported by Buckles[16]) are substituted into these three correlations, the following solubility predictions are obtained: the Wabasca correlation predicts 0.64% (wt.), the Peace River correlation predicts 0.61%, and the Athabasca correlation predicts 0.47%. This indicates that the methane is more soluble in Cold Lake bitumen than in any of the other bitumens, and that the Wabasca bitumen is the most similar to Cold Lake bitumen with regard to methane solubility. Therefore, it was decided to adapt the Wabasca correlation to the Cold Lake bitumen by modifying the constant in order to fit the one observed solubility. Hence, for Cold Lake bitumen,

$$\log_{10}\left(\frac{\tilde{x}_m}{P}\right) = -1.00 + \frac{110}{T} - 0.010\,P$$

At T=286.15°*K*., P=3.10 MPa, this correlation predicts a solubility of 0.70% (wt.), which is close enough to what was observed.

This correlation should be regarded as a tentative estimate, until direct experimental data become available.

5.5 References for Chapter 5

1. anonymous, "*Geology and proved in place reserves of the Cold Lake oil sands deposits*", (Energy Resources Conservation Board, Calgary, 1973).

2. D. Jardine, "Cretaceous Oil Sands of Western Canada", pp. 50-67, in L.V. Hills ed., "*Oil Sands, Fuel of the Future*", (Canadian Society of Petroleum Geologists, Calgary, 1974).

3. Douglas F. Minken, "The Cold Lake Oil Sands: Geology and a Reserves Estimate", pp. 84-99, in "*Oil Sands, Fuel of the Future*", op. cit.

4. A.G. Winestock, "Developing A Steam Recovery Technology", pp. 190-198,

in "*Oil Sands, Fuel of the Future*", op. cit.

5. S.A. Pursley, "Experimental studies of thermal recovery processes", *Symposium on Heavy Crude Oil*, Maracaibo, Venezuela, July 1974.

6. S.M. Farouq-Ali:

6a. "Application of In Situ Methods of Oil Recovery to Tar Sands", pp. 199-211, in "*Oil Sands, Fuel of the Future*", op. cit.

6b. "Current Status of Steam Injection as a Heavy Oil Recovery Method", *Journal of Canadian Petroleum Technology* **13**(1), 54-68 (January-March 1974).

6c. Reference #7.

7. S.M. Farouq-Ali, "Current Status of In-Situ Recovery From the Tar Sands of Alberta", *Journal of Canadian Petroleum Technology* **14**(1), 51-58 (January-March 1975).

8. K.H. Coats, "Simulation of Steamflooding With Distillation and Solution Gas", *Society of Petroleum Engineers Journal* **16**, 235-247 (1976).

9. R.G. Finbow and I.J. Koop, "A sensitivity study of cyclic steam stimulation using a 2-D mathematical model", pp. 419-433, in David A. Redford and Alvin G. Winestock eds., "*The Oil Sands of Canada Venezuela 1977*", CIM Special Volume 17, (The Canadian Institute of Mining and Metallurgy, 1977); also published in *Journal of Canadian Petroleum Technology* **17**(2), 58-72 (April-June 1978).

10. G.H. Kendall and D.E. Towson, "Importance of Reservoir Description in Evaluating In-Situ Recovery Methods for Cold Lake Heavy Oil",
Part I - "Reservoir Description", G.H. Kendall,
Part II - "In-Situ Application", D.E. Towson,
Journal of Canadian Petroleum Technology **16**(1), 41-54 (January-March 1977); *Bulletin of Canadian Petroleum Geology* **25**(2), 314-340 (May 1977).

11. George T. MacCallum, "Emerging Geology of the Heavy-Oil Sands", *Bulletin of Canadian Petroleum Geology* **25**(2), 305-313 (May 1977).

12. J.H. Nicholls and R.W. Luhning, "Heavy Oil Sand In-Situ Pilot Plants in Alberta (Past and Present)", *Journal of Canadian Petroleum Technology* **16**(3), 50-61 (July-September 1977).

13. O.P. Strausz, "The Chemistry of the Alberta Oil Sand Bitumen", pp. 146-153, in David A. Redford and Alvin G. Winestock eds., "*The Oil Sands of Canada Venezuela 1977*", CIM Special Volume 17, (The Canadian Institute of Mining and Metallurgy, 1977).

14a. H.G. Weinstein, J.A. Wheeler, and E.G. Woods, "Numerical Model for Thermal Processes", *Society of Petroleum Engineers Journal* **17**, 65-78 (1977).

14b. H.G. Weinstein, "Mathematical models for thermal recovery processes", *Symposium on Heavy Crude Oil*, Maracaibo, Venezuela, July 1974.

15. Jacques G. Burger, "In-situ recovery of oil from oil sands", chapter 8 in G.V. Chilingarian and T.F. Yen eds., "*Bitumens, Asphalts, and Tar Sands*", (Elsevier, Amsterdam, 1978).

16. R.S. Buckles, "Steam Stimulation Heavy Oil Recovery at Cold Lake, Alberta", paper SPE 7994, presented at the Society of Petroleum Engineers of AIME 49th California Regional Meeting, Ventura, April 18-20, 1979.

17. John M. Dealy, "Rheological Properties of Oil Sand Bitumens", *Canadian Journal of Chemical Engineering* **57**(6), 677-683 (December 1979).

18. S.M. Farouq-Ali and R.F. Meldau, "Current Steamflood Technology", *Journal of Petroleum Technology* **31**, 1332-1342 (1979).

19. S.M. Farouq-Ali, private communication, 1979, referenced by R.F. Meldau, R.G. Shipley, and K.H. Coats, "Cyclic Gas/Steam Stimulation of Heavy-Oil Wells", *Journal of Petroleum Technology* **33**, 1990-1998 (1981).

20. George R. Jenkins and John W. Kirkpatrick, "Twenty years' operation of an in-situ combustion project", *Journal of Canadian Petroleum Technology* **18**(1), 60-66 (January-March 1979).

21. G.S. Reddy, D.R. Prowse, and D.A. Redford, "Physical Modeling and Numerical Simulation of In Situ Recovery of Bitumen from Oil Sands by Steam Injection", paper No. 80-31-10, 31st Annual Technical Meeting, Petroleum Society of CIM, Calgary, May 1980.

22. R.R. Capeling and J.K. Peggs, "Experimental Steamflood. Cold Lake Oil Sands", pp. 361-368, in R.F. Meyer, C.T. Steele, and J.C. Olson eds., "*The Future of Heavy Crude Oils and Tar Sands*", First International Conference, United Nations Institute for Training and Research (UNITAR), (McGraw-Hill, New York, 1981).

23. J.W. Grabowski, B. Rubin, and T.G. Harding, "A preliminary numerical simulation study of in-situ combustion in a Cold Lake oil sands reservoir", *Journal of Canadian Petroleum Technology* **20**(2), 79-89 (April-June 1981).

24. G.D. Mossop et al., "Geology of Alberta's Oil Sands and Heavy Oil Deposits", pp. 197-207, in "*The Future of Heavy Crude Oils and Tar Sands*", First International Conference, op. cit.

25. A. Settari and J.M. Raisbeck, "Analysis and Numerical Modeling of Hydraulic Fracturing During Cyclic Steam Stimulation in Oil Sands", *Society of Petroleum Engineers Journal* **21**, 2201-2212 (1981).

26. J. Skrabec, "Process Selection Considerations in the Upgrading of Cold Lake Bitumen", pp. 612-617, in "*The Future of Heavy Crude Oils and Tar Sands*", First International Conference, op. cit.

27. J. Starr, J.M. Prats, and S.A. Messulam, "Chemical Properties and Reservoir Characteristics of Bitumen and Heavy Oil From Canada and Venezuela", pp.

168-173, in "*The Future of Heavy Crude Oils and Tar Sands*", First International Conference, op. cit.

28. Walter Ruehl, "*Tar (Extra Heavy Oil) Sands and Oil Shales*" (English translation), volume 6 of Heinz Beckmann ed., "Geology of Petroleum", (Ferdinand Enke Publ., Stuttgart, 1982).

29. M.M. Schumacher ed., "*Heavy Oil and Tar Sands Recovery and Upgrading--International Technology*", (Noyes Data Corporation, Park Ridge, NJ, U.S.A., 1982), pp. 271,272, and 341.

30. Maurice A. Carrigy, "Thermal Recovery from Tar Sands", *Journal of Petroleum Technology* **35**(13), 2149-2157 (1983).

31. Donald Towson, "Tar Sands", "*Kirk-Othmer Encyclopedia of Chemical Technology*", 3rd edition, (Wiley-Interscience, New York, 1983).

32. Glenn G. Mainland and Hing Y. Lo, "Technological Basis for Commercial In Situ Recovery of Cold Lake Bitumen", pp. 235-242, in *Proceedings of the 11th World Petroleum Congress*, London, U.K., 1983, (Wiley & Sons, Chichester, U.K., 1984).

33. R. Steinborn and D.L. Flock, "The rheology of heavy crude oils and their emulsions", *Journal of Canadian Petroleum Technology* **22**(5), 38-52 (September-October 1983).

34. D.R. Babu, V. Hornof, and G. Neale, "Effects of Temperature and Time on Interfacial Tension Behavior Between Heavy Oils and Alkaline Solutions", *Canadian Journal of Chemical Engineering* **62**(1), 156-159 (February 1984).

35. J.H. Duerksen, G.W. Cruikshank, and M.L. Wasserman, "Performance and Simulation of a Cold Lake Tar Sand Steam-Injection Pilot", *Journal of Petroleum Technology* **36**, 1781-1790 (1984).

36. Maurice B. Dusseault and Hans R. Van Domselaar, "Unconsolidated sand

sampling in Canadian and Venezuelan oil sands", pp. 336-348, in R.F. Meyer, J.C. Wynn, and J.C. Olson eds., "*The Future of Heavy Crude and Tar Sands*", 2nd International Conference, United Nations Institute for Training and Research (UNITAR), (McGraw-Hill, New York, 1984).

37. S.M. Farouq-Ali, "Steam Injection--Theory and Practice", pp. 49-68, in Ender Okandan ed., "*Heavy Crude Oil Recovery*", (Martinus Nijhoff Publishers, The Hague, Netherlands, 1984).

38. The molecular weight in table 5.1 is calculated from an "average" molecular formula contained in M.A.B. Khan, A.K. Mehrotra, and W.Y. Svrcek, "Viscosity models for gas-free Athabasca bitumen", *Journal of Canadian Petroleum Technology* **23**(3), 47-53 (May-June 1984).

39. G.S. Reddy, D.M. Adams, and R.F. Meldau, "Summary of Enhanced Oil Recovery Pilots for Oil Sands and Heavy Oil in Canada", pp. 1041-1062, in R.F. Meyer, J.C. Wynn, and J.C. Olson eds., "*The Future of Heavy Crude and Tar Sands*", 2nd International Conference, United Nations Institute for Training and Research (UNITAR), (McGraw-Hill, New York, 1984).

40. W.R. Shu and V.N. Venkatesan, "Kinetics of thermal visbreaking of a Cold Lake bitumen", *Journal of Canadian Petroleum Technology* **23**(2), 60-64 (March-April 1984).

41. Anil K. Mehrotra and William Y. Svrcek, "Correlations for properties of bitumen saturated with CO2, CH4 and N2, and experiments with combustion gas mixtures", *Journal of Canadian Petroleum Technology* **21**(6), 95-104 (November-December 1982).

42. William Y. Svrcek and Anil K. Mehrotra, "Gas solubility, viscosity and density measurements for Athabasca bitumen", *Journal of Canadian Petroleum Technology* **21**(3), 31-38 (July-August 1982).

43. Anil K. Mehrotra and William Y. Svrcek, "Viscosity, Density and Gas Solubility Data for Oil Sand Bitumens. Part II. Peace River Bitumen Saturated with N2, CO, CH4, CO2 and C2H6", *AOSTRA Journal of Research* **1**(4), 269-279 (June 1985).

44. Anil K. Mehrotra and William Y. Svrcek, "Viscosity, Density and Gas Solubility Data for Oil Sand Bitumens Part III: Wabasca Bitumen Saturated with N2, CO, CH4, CO2 and C2H6", *AOSTRA Journal of Research* **2**(2), 83-93 (December 1985).

45. Maurice B. Dusseault, "Sample disturbance in Athabasca oil sand", *Journal of Canadian Petroleum Technology* **19**(2), 85-92 (April-June 1980).

46. R.M. Butler, "The expansion of tar sands during thermal recovery", paper No. 85-36-24, 36th Annual Technical Meeting, Petroleum Society of CIM, Edmonton, June 2-5, 1985.

47. Kenneth Denbigh, "*The Principles of Chemical Equilibrium*", 3rd edition, (Cambridge University Press, Cambridge, U.K.).

48. D.H. Burger, R.A. Heidemann, and K.Aziz, "A computer file of oil reservoir fluid property data", *Journal of Canadian Petroleum Technology* **17**(2), 92-99 (April-June, 1978).

6. RESULTS AND CONCLUSIONS

6.1 Results

Only preliminary results from the two-dimensional front-tracking simulator can be presented in this report due to several restrictions which limit the simulator at present. During any realistic simulation, the set of line segments representing the steam front will sweep past stationary grid points. For example, a stationary grid point might be outside the steam zone at one time level, and inside the steam zone at the next time level, because the steam zone has expanded. When this happens, the grid block structure is drastically changed, and significant regions are transferred from one grid block to another. The simulator, at present, does not have the capability to calculate these area transfers, and to account for the effect of these transfers on the discretized equations. However, at present, the simulator *does* have the ability to handle the restricted class of simulations in which each front-tracking point is limited to the line segment (joining two stationary grid points) on which it was originally located, and can track the movement of the steam front subject to this limitation.

A further restriction on the simulator is that if there is a steam front, there should be at least two stationary grid points on each side of the steam front. If there is only one stationary grid point on one side of the steam front, and especially if this stationary grid point is at one of the corners of the simulation domain, there may be a tendency in the Jacobian for the columns associated with the motion of adjacent front-tracking points to be linearly dependent. Such a linear dependence would mean that there exists no well-defined solution for the location of the front-tracking points (basically because the grid is too coarse). Such a linear dependence also would cause the Jacobian to be singular, thus incapacitating the simulator. Until this problem is investigated further, it is prudent to assume that this restriction is necessary, especially since this is not a

serious limitation of the simulator.

The simulator was tested using a test problem (see figure 6.1) in which the reservoir is 80 m long and 30 m deep. The second horizontal dimension is assumed infinite. Steam of 97% quality (by volume) is injected at constant pressure (1.379×10^6 Pa) through a section of the reservoir border extending from one of the bottom corners to a point 10 m above that corner, according to this test problem. Reservoir fluids are produced at constant pressure (5.17×10^5 Pa) through a section of the reservoir border extending from the top corner directly above the injection zone to a point 5m below that corner. The no-flow boundary condition is imposed on the rest of the boundary of the region. With the exception of the light oil mole fraction, the physical properties of the fluids and the reservoir are the same as those used by Coats[1] in his second sample problem, and by the present authors in part I of this report.

A regular 3 x 4 array of grid points was chosen as the finite-difference grid so that the vertical spacing between rows of grid points was 10 m, and the horizontal spacing was 40 m. The grid blocks into which the simulation domain was partitioned (at t=0) was shown in figure 6.2. Since the simulator cannot handle grid blocks with zero area, the initial location of the steam front was taken to be not at the border of the simulation domain, but rather a short distance inside. In particular, the initial locations of the intersection points of the steam front with the three grid lines which it crosses were taken to be at (79.72,0.00), (79.76,10.00), and (80.00,10.12)

When the initial mole fraction of volatile oil (x_1) was set to 0.30, the value used by Coats[1] in his second sample problem, the simulator did not work for reasons which we have not yet been able to trace. However, the simulator gave reasonable-looking results when the initial x_1 was set to either 0.01 or to 0.00.

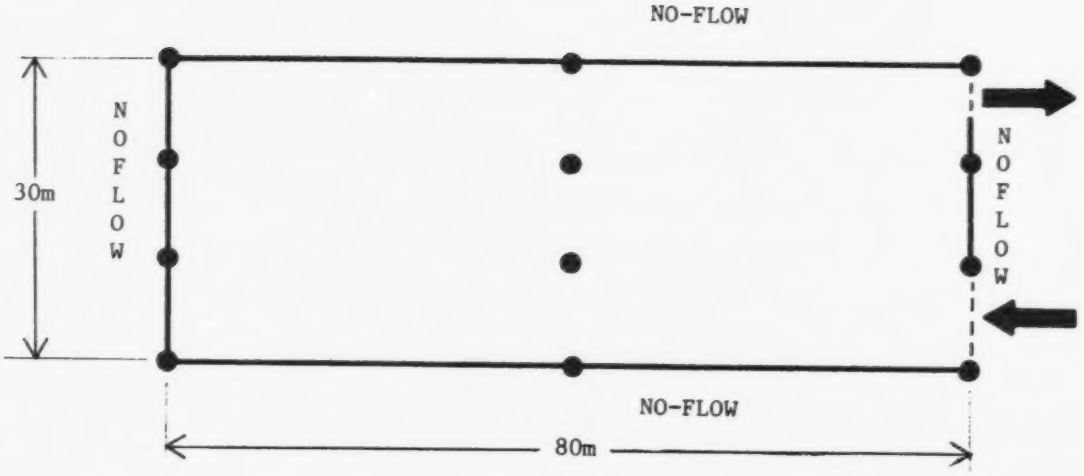

FIGURE 6.1. A test problem for the simulator.

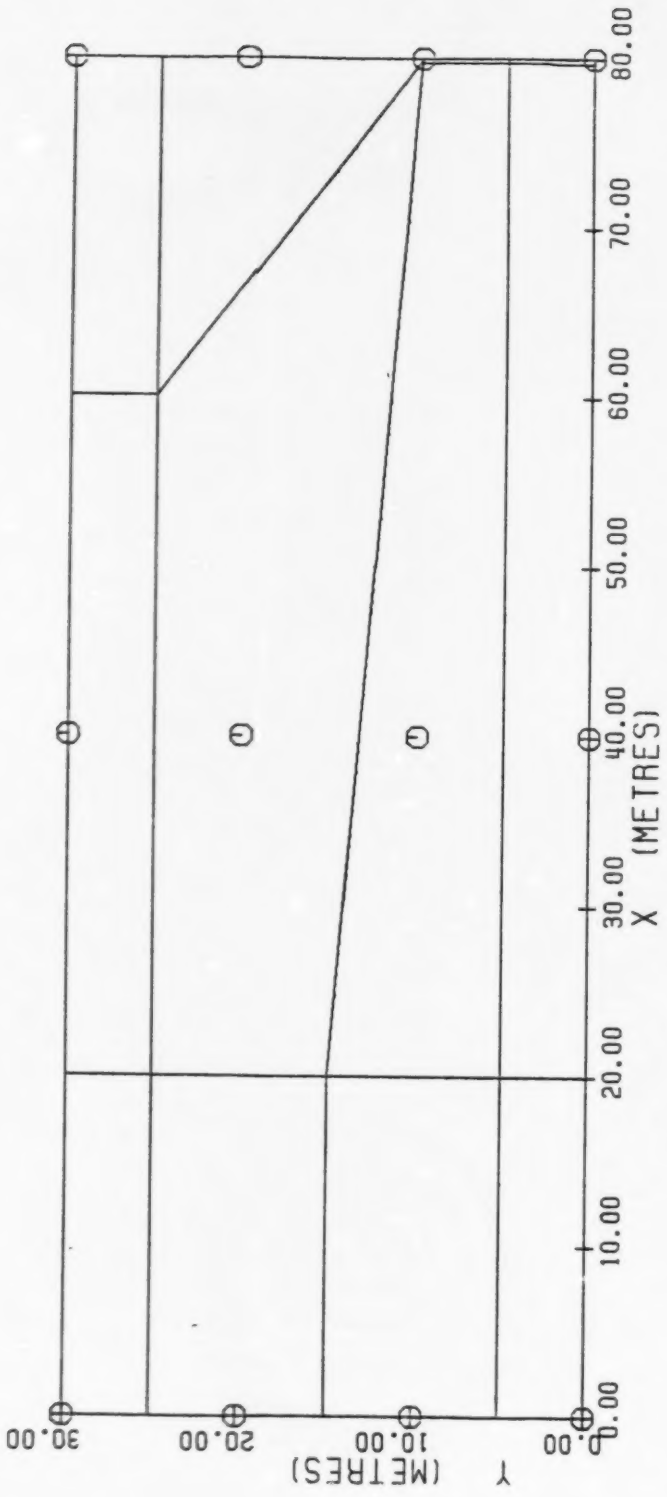

FIGURE 6.2. The grid blocks at t = 0 for the sample problem.

As expected, the simulator calculated that the steam zone expands most quickly along the direct path from the injection zone to the production zone. During the period of time in which the steam zone advances almost 10 m in the vertical direction, it advances less than 0.3 m in the horizontal direction. The expansion of the steam zone in the vertical direction is shown in figure 6.3. There is very little difference between the results for $(x_1)_{initial} = 0.01$ and $(x_1)_{initial} = 0.00$. The speed with which the steam zone advances (an elapsed time of 60,000 seconds is an unusually short period of time for a steam injection project) may be attributed to the short distance between the injection and production zones, and to the relatively low viscosity of the oil. The curvature in the plots in figure 6.3 may be attributed to impending breakthrough by the steam. As was indicated previously, the crossing of stationary grid points by the steam front will be possible only with the further development of the simulator.

One problem which has plagued the development of this simulator is the problem of ill-conditioned Jacobians. There are several things that can cause this problem, and several precautions that have been taken. One fundamental factor that can cause a Jacobian to be ill-conditioned is the significant difference between the time scale of the pressure changes and the time scale of the saturation changes. As was discussed in section 4.7, various linear combinations of the balances were chosen in order to resolve this problem. As is discussed above, the restriction that there be at least two stationary grid points on each side of the steam front (assuming that there is a steam front) is another precaution against ill-conditioned Jacobians. Another possible cause is the matching conditions at the steam front. It is suspected that the matching conditions which are currently being used may be contributing to the problem. Although attempts have been made to find matching conditions which do not cause the Jacobians to be ill-conditioned, these alternate matching conditions have problems which appear to

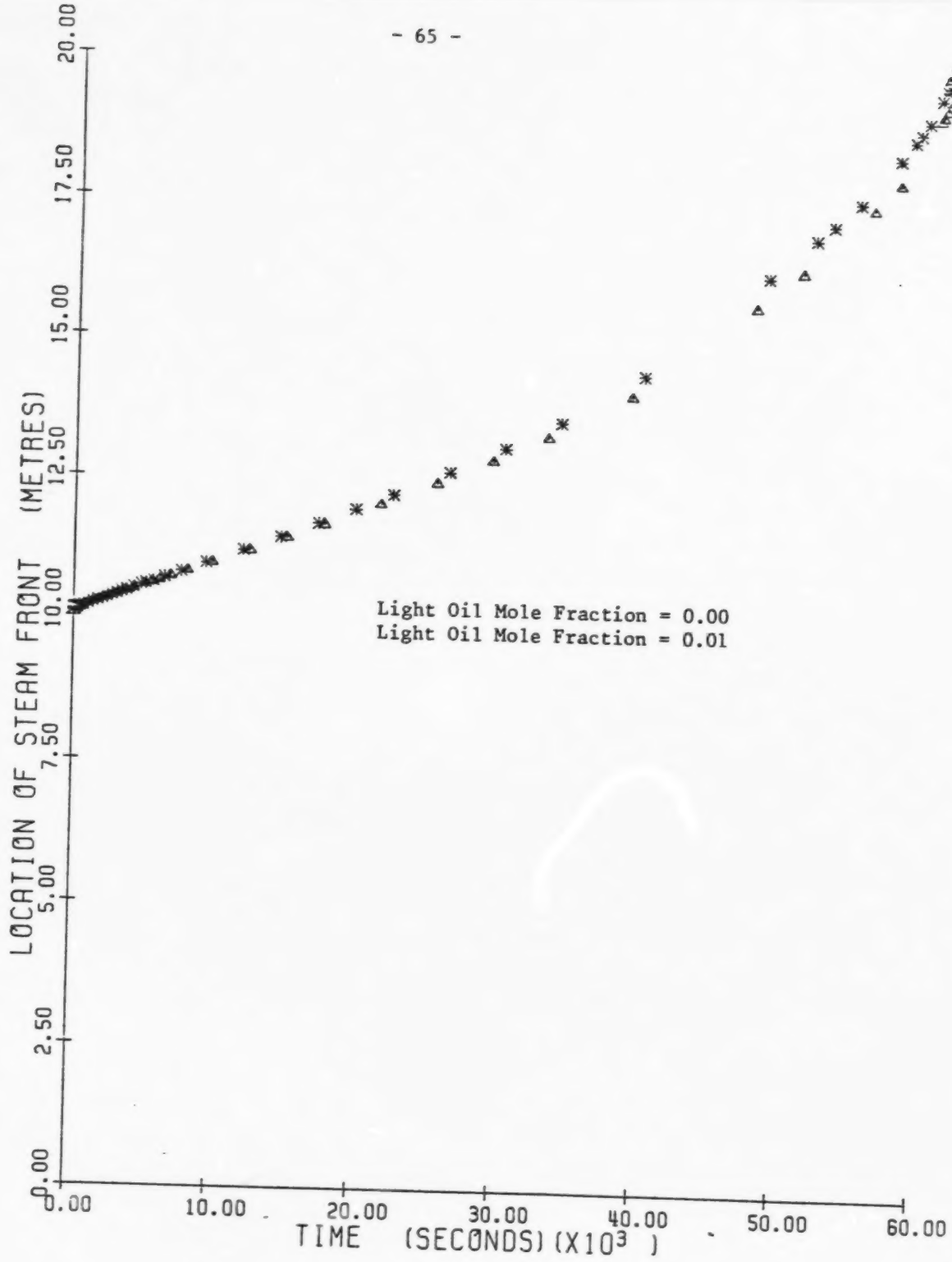

FIGURE 6.3. The height of the steam zone as a function of time.

be even more serious. Finally, a poor starting guess for the unknowns at a given time level may cause a Jacobian to be ill-conditioned. This problem can often be resolved by repeating the time step with a smaller time step size and/or a different starting guess for the unknowns. Despite the precautions which have already been taken to prevent the Jacobians from being ill-conditioned, further work should be done to investigate this problem, and to develop better methods for resolving this problem.

6.2. Conclusions

The front-tracking simulator can track the movement of a steam front, provided that the steam front does not sweep over a stationary grid point. The method for specifying the location of the steam front and for partitioning the simulation domain into grid blocks is quite flexible. Since the method tracks the steam front along both horizontal and vertical grid lines, it can handle steam fronts with a wide variety of shapes.

By using this method combined with suitable matching conditions and a set of discretized governing equations, the simulator has demonstrated the ability to describe, over a limited period of elapsed time, the expansion of the steam zone which results when steam is injected into a cold, heavy oil reservoir. Although there are several factors which can cause the Jacobian to be ill-conditioned, the precautions which have been developed to resolve this problem are adequate for some simulations. Further work is required to either assess more precisely the effectiveness of these precautions, or to develop better computation strategies.

The most significant limitation on the 2-D simulator is the inability to track the motion of the steam front as it sweeps over a stationary grid point. This is not a fundamental limitation of the simulator: it can be removed with a moderate amount of additional work.

6.3 Reference for Chapter 6

1. K.H. Coats, "A Highly Implicit Steamflood Model", *Society of Petroleum Engineers Journal* **18**, 369-383 (1978).

NOMENCLATURE

A_{ij} area of grid block i,j

δA^n_{ijkl} size of area transfer to grid block i,j from block k,l during time step n

b_{ij} boundary of grid block i,j

c_p heat capacity

$\underline{F}$ functional relation among unknowns

g acceleration due to gravity

h enthalpy

J Jacobian

k absolute permeability

k_r relative permeability

k_{rw} relative permeability of the water phase

k_{row} relative permeability of the hydrocarbon phase with respect to the water phase

k_{rg} relative permeability of the vapour phase

k_{rog} relative permeability of the hydrocarbon phase with respect to the vapour phase

M condensation rate

$\underline{n}$ unit vector normal to a line or curve

N_F number of front-tracking points

N_X number of stationary grid points in the X-direction

N_Y number of stationary grid points in the Y-direction

P pressure

s arc length

S saturation

t time

T temperature

U generalized vector of unknowns

w mole fraction in a deliberately unspecified phase

x mole fraction in the (liquid) hydrocarbon phase

$\hat{x}_m$ weight fraction of methane in bitumen

X horizontal position

y mole fraction in the vapour phase

Y vertical position

α compressibility

β coefficient of thermal expansion

δ change

λ mobility

μ viscosity

ρ density

τ transmissibility

ϕ porosity

Φ pressure minus hydrostatic pressure

Subscripts

A Athabasca

c component

C Cold Lake

g gas/vapour

irr irreducible

i X-direction

j Y-direction

k X-direction

l Y-direction

m front-tracking point or methane depending on context

o oil/hydrocarbon

OB overburden

p phase

r rock/reservoir matrix

w water (liquid)

Superscripts

k iteration level

n time level

APPENDIX

In the main body of the report, the integrals on the right side of equations (4.15) and (4.16) were approximated with a relatively straightforward approximation for the normal component of the pressure gradient, $-\underline{\nabla}\Phi_p \cdot \underline{n}$. Originally, a higher-order approximation for these terms was formulated. However, it was abandoned, in favour of the simpler version, due to the severe spatial oscillations in pressure, in the region adjacent to the steam zone, caused by this formulation. This appendix explains how the higher-order approximation was constructed.

The higher-order approximation is based on a weighted average of two approximate values of the normal component of the pressure gradient, computed at two points. The locations of the two points depend on the position and orientation of the edge segment with respect to the steam front. Fourteen separate cases are distinguished in the simulator. However, for the purposes of this explanation, it is convenient to count any pair of cases which differ only by 90^o or 180^o rotations as equivalent. Thus, it suffices to consider five essentially different cases. Figure A.1 presents a detailed description of how each of the five cases is handled. In particular, the two points at which the approximate values of $-\underline{\nabla}\Phi_p \cdot \underline{n}$ are evaluated are labeled C0 and Cl in each of the five diagrams in figure A.1.

The method for calculating approximate values for the normal component of the pressure gradient exploits the fact that if the pressure is known at three grid points (and these three grid points do not lie on a straight line), then it is possible to construct a linear function of the form

$$P = c_{00} + c_{10}X + c_{01}Y \qquad \text{(A.1)}$$

such that the values of the function at the three grid points are exactly equal to the given pressures. In the following paragraphs, this function is denoted as "*the linear interpolation of the pressure*" through the three grid points. From this function (A.1), the pressure gradient may be readily computed.

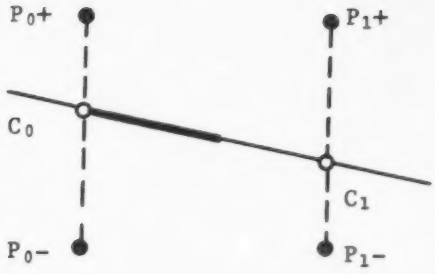

a non-front edge which does not touch a front edge

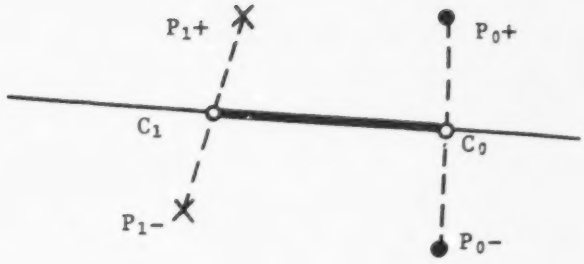

a non-front edge which touches a front edge

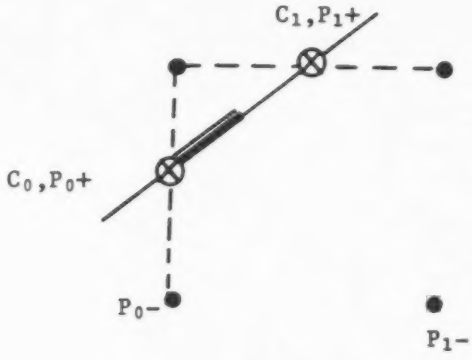

the partner of a front edge which forms part of a triangle together with two intersecting grid lines

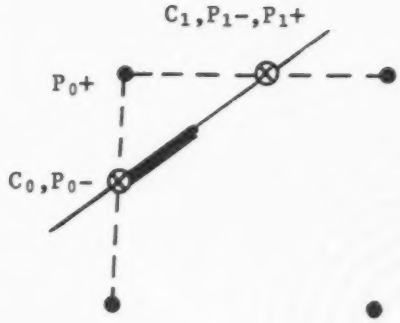

a front edge which forms part of a triangle together with two intersecting grid lines

Figure A.1: The location of the points used to calculate the flows across an interior edge. Five essentially different cases. (continued on next page)

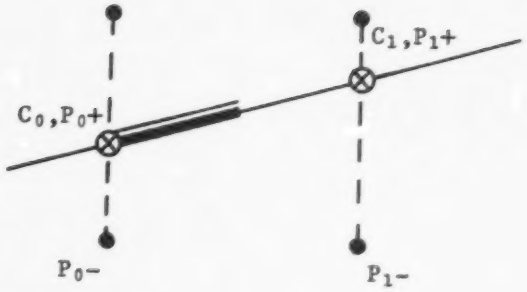

a front edge which forms part of a quadrilateral together with three gridlines.

———	the edge across which the flow is being calculated
═══	a front edge and its partner
———	the line containing the edge
– – – –	a line drawn to show that certain points are collinear
•	a stationary grid point
×	a moving grid point
○	a point at which the normal pressure gradient component is evaluated
⊗	o and x coincide

Figure A.1 (cont.)

According to the nomenclature of figure A.1, the pressure gradient at point C0 is calculated to be the arithmetic mean of the pressure gradient obtained from the linear interpolation of the pressure through points $P0^-$, $P0^+$ and $P1^-$, and the pressure gradient obtained from the linear interpolation of the pressure through points $P0^-$, $P0^+$ and $P1^+$. (Points $P0^-$ and $P0^+$ should never coincide.) Likewise, the pressure gradient at point C1 is calculated to be the arithmetic mean of the pressure gradient obtained from the linear interpolation of the pressure through points $P1^-$, $P1^+$ and $P0^-$, and the pressure gradient obtained from the linear interpolation of the pressure through points $P1^-$, $P1^+$ and $P0^+$, provided that points $P1^-$ and $P1^+$ do not coincide. If they do coincide, then the pressure gradient at C1 is assumed to be the same as the pressure gradient at C0. Figure A.1 shows how the grid points $P0^-$, $P0^+$, $P1^-$, and $P1^+$ are chosen in each of the five different cases. The resulting formulae are rather complicated, but are straightforward to derive; hence, they are not included in this report.

The weights of the weighted average referred to in the second paragraph of this ("Interior Edge Segments") section may be determined by approximating the integral (over an interior edge segment)

$$\int -\underline{\nabla}\Phi_p \cdot \underline{n}\, ds$$

with the integral of an interpolating function of the form

$$-\underline{\nabla}\Phi_p \cdot \underline{n} \approx d_{00} + d_{10}X + d_{01}Y \qquad \text{(A.2)}$$

which is chosen so that the values of the interpolating function (A.2) at points C0 and C1 are exactly equal to the approximate values of $-\underline{\nabla}\Phi_p \cdot \underline{n}$, which have been calculated according to the procedure described above. Although the interpolating function is not unique, the value of the integral *is* unique, and may be expressed as the weighted average of the approximate values of $-\underline{\nabla}\Phi_p \cdot \underline{n}$ at points C0 and C1. Thus, the weights of the weighted average are determined. Once

again, since the formulae for these weights are rather complicated, but are readily derived, they are not given in this report.

This method of calculating the flow terms is considerably more complicated than the methods which are generally used. One reason for the extra complexity is to avoid grid-orientation effects, which are believed (e.g. by Yanosik and McCracken[1]) to be caused by crude approximations for the flow terms. The second reason for the extra complexity is the presence of non-rectangular grid blocks; if all the grid blocks were rectangular, the formulae described above would be considerably simpler.

Reference for Appendix

1. Y.L. Yanosick, T.A. McCracken, "A Nine-Point, Finite-Difference Reservoir Simulator for Realistic Prediction of Adverse Mobility Ratio Displacements", *Society of Petroleum Engineers Journal* **19**, 253-262 (1979).